

**RESEARCH ARTICLE**

WILEY

Mafic volcanic rocks of western Iron Ore Group, Singhbhum Craton, eastern India: Geochemical evidence for ocean–continent convergence

Madhuparna Paul¹ | Jyotiskar Ray¹ | C. Manikyamba² | Sohini Ganguly³ | M. Rajanikanta Singh² | Saraswati Pachal¹ | Debaleena Sarkar¹¹Department of Geology, University of Calcutta, Kolkata, India²National Geophysical Research Institute (Council of Scientific and Industrial Research), Hyderabad, India³School of Earth, Ocean and Atmospheric Sciences, Goa University, Taleigao Plateau, Goa, India**Correspondence**Jyotiskar Ray, Department of Geology, University of Calcutta, 35 Ballygunge Circular Road, Kolkata 700019, India.
Email: jsray65@hotmail.com**Funding information**

Department of Science and Technology, Grant/Award Number: SR/S4/ES-510/2010; GeoMet, Grant/Award Number: MLP 0002 FBR2-EVSSKB

Handling Editor: N.V. Chalapathi Rao

Precambrian mafic magmatism is an important global episode which played a significant role in the crustal evolution. In India, Singhbhum Craton being the oldest craton, witnessed significant occurrences of Precambrian geological activity, marked by several episodes of volcanism, plutonism, sedimentation spanning from Palaeoarchean to Mesoproterozoic age. Here we present petrological and geochemical characteristics of Precambrian mafic volcanic rocks (occurring in western Iron Ore Group (IOG), Singhbhum Craton, eastern India) to evaluate their petrogenetic aspects, tectonic setting, and magma generation. The mafic volcanic rocks are porphyritic in nature with the phenocrysts of plagioclase and groundmass composed of clinopyroxene, plagioclase, ilmenite, and volcanic glass. These rocks are mostly tholeiitic, sometimes with a transitional behaviour towards calc-alkaline nature and display basalt-basaltic andesite affinity. These mafic volcanic rocks also preserve geochemical signatures (high Nb/U, Nb/La, [Nb/Th]_{pm} ratios) in support of Nb-enriched basalts and are classified as Nb-enriched basalts (NEB; Nb > 7 ppm) and high-Nb basalts (HNB; Nb > 20 ppm) on the basis of Nb concentrations and mantle normalized Nb/La ratios (>0.5). The NEBs and HNBS are marked by lesser magnitude of negative Nb anomalies with high (Nb/Th)_{pm}, (Nb/La)_{pm}, and Nb/U ratios as compared to normal arc basalts. Several major element oxides, trace elements, and selected element ratios (like SiO₂, CaO/Al₂O₃, Y, V/Cr, Zr/Nb, and \sum REE) show systematic variations with MgO which suggests role of magmatic fractionation. Chondrite-normalized REE patterns for NEB and HNB rocks exhibit uniform LREE enrichment with distinct Eu negative anomalies while primitive mantle-normalized incompatible trace element patterns reflect enrichment in LILE and LREE with prominent Nb-Ta anomalies. Different HFSE ratios corroborate a subduction related setting for magma generation formed by ~10%–20% melting in the domain of garnet lherzolite. Relative enrichment of LILE and LREE with depleted HFSE characteristics attest a garnet-bearing mantle source and melt extraction with garnet in the residue. Geochemical signatures suggest that the genesis of NEB and HNB is attributable to slab-melting and wedge hybridization processes

during matured stages of subduction. Selected incompatible trace element ratios for the studied mafic volcanic rocks invoke an enriched (EM1-EM2 type) mantle source and unequivocally suggest effects of continental crustal assimilation of the parent magma. Liquid immiscibility has played an important role as a differentiation mechanism leading to presence of high and low FeO types. The IOG mafic volcanic rocks preserve distinct geochemical signatures of matured stage of subduction, slab melting, crustal contamination and magma generation at an Archean ocean–continent convergent margin setting.

KEYWORDS

calc-alkaline affinity, crustal contamination, liquid immiscibility, Nb-enriched basalts, Singhbhum Craton, slab melting

1 | INTRODUCTION

Precambrian cratons around the world comprise distinct lithological associations that preserve evidence of episodic continental growth spanning from 4.0–2.5 Ga through vertical and lateral accretion of juvenile crustal materials under diverse geodynamic conditions at oceanic and continental realms (Condie, 2005; Polat, Hofmann, & Rosing, 2002; Polat & Kerrich, 2006; Polat, Kerrich, & Wyman, 1999; Santosh, 2013; Srivastava & Ahmad, 2008). It has been envisaged that around 70%–80% of the continental crust had been generated prior to 2.5 Ga with a peak at 2.7 Ga (Komiya et al., 2017; Zhai, 2014). Viable models for lateral growth of Precambrian continental crust espouse accretion of arc magmas through subduction–collision processes at active continental margins and accretion of island arc and oceanic plateaus to form microcontinents. However, mantle plume activities in terms of ocean island basalts (OIB), oceanic plateau basalts (OPB), continental flood basalts (CFB), and underplating of mantle-derived melts beneath lower crust account for vertical crustal growth (Bédard, 2018; Condie, 1999; Manikyamba, Ganguly, Santosh, & Subramanyam, 2017; Pahari et al., 2019; Turkina & Nozhkin, 2003; Wyman, 2018). Precambrian mafic magmatism represents major thermal events in the evolutionary history of the earth with dynamic mantle melting and melt extraction processes that contributed to the crust generation mechanisms. Precambrian magmatic episodes were associated with diverse tectonic environments including: (a) an oceanic plateau association composed of compositionally uniform komatiites and Mg- to Fe-rich tholeiitic basalts erupted from mantle plumes, (b) a compositionally diverse oceanic and continental arc associations, dominated by “normal” tholeiitic to calc-alkaline basalts, andesites, dacites, and rhyolites with boninites, picrites, low-Ti tholeiites, adakites, high-magnesian andesites, and Nb-enriched basalts, and (c) ultramafic-mafic-alkaline lithologies indicating plume magmatism at rifted cratonic margins (Manikyamba et al., 2017; Polat & Kerrich, 2006). The Archean era (4.0–2.5 Ga) was marked by episodic cycles of volcanism and sedimentation that led to the formation of greenstone belts. The Archean greenstone belt has been customarily attributed either to plume-tectonics (with dominant

intraplate magmatism in oceanic plateau) or subduction tectonics with volcanism at convergent plate margins. In some case, however, combination of these two processes (involving both plume tectonics and plate tectonics) has also been suggested (Condie, 2001). The origin and evolution of Archean granite-greenstone belts are subjects of immense interest in understanding the mantle processes, crustal growth, and tectonic evolution of the early Earth. Particularly, the volcanic supracrustals of greenstone belts represent magmatic episodes associated with Precambrian terrane accretion, continental lithosphere evolution and crustal growth through subduction–accretion processes, plume–arc cohabitation, plume–craton interactions, and arc–continent collisions (Barnes & Van Kranendonk, 2014; Dostal & Mueller, 2013; Ganguly, Santosh, & Manikyamba, 2019; Ganguly & Yang, 2018; Ghose & Saha, 2018; Manikyamba et al., 2017; Manikyamba & Kerrich, 2012; Ray et al., 2013; Smithies, Champion, Van Kranendonk, Howard, & Hickman, 2005). Mafic magmatism associated with Precambrian Large Igneous Provinces (LIPs; Mc Call, 2003; Rey, Philippot, & Thebaud, 2003; Sylvester, Campbell, & Bowyer, 1997) as exemplified in Black Range Dyke Swarms in Pilbara Craton, Australia (Heaman, 2008; Wingate, 1999), Mackenzie LIP in northwest Canada (Heaman & LeCheminant, 1993; LeCheminant & Heaman, 1989), Garder Province of southern Greenland (Upton, Emeleus, Heaman, Goodenough, & Finch, 2003) and Dalarna complex in central Scandinavia (Soderlund, Elming, Ernst, & Schissel, 2006; Suominen, 1991), and numerous Phanerozoic equivalents (Coffin & Eldholm, 1994; Heaman, 2008) are characterized by voluminous magmatic pulses in short durations and giant dyke swarms that served as transport systems for mantle-derived magmas. These provide ideal markers to constrain episodes of continental reconstructions and crustal growth (Bleeker & Ernst, 2006; Harlan, Heaman, LeCheminant, & Premo, 2003).

The geological history of the Singhbhum Craton of eastern India is marked by several episodes of volcanism, plutonism, and sedimentation spanning from Palaeoarchean to Mesoproterozoic in a dynamic tectonic realm. Moreover, distinct signatures of Archean-Proterozoic geodynamic processes are preserved in discrete crustal provinces in this craton (Bose, 2000; Eriksson, Mazumder, Catuneanu, Bumby, &

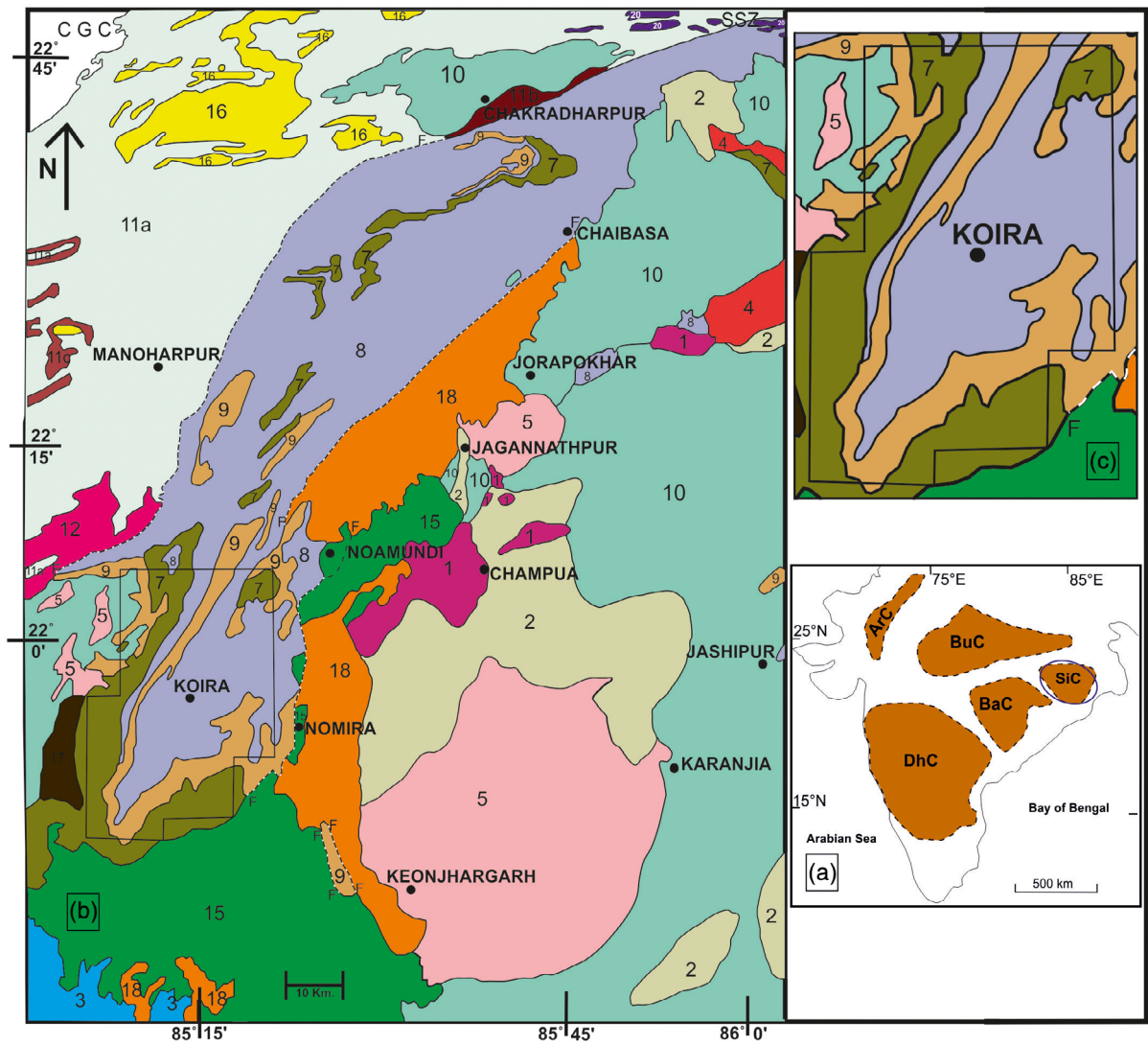
Ountsche Ilondo, 2006; Misra, 2006; Mukhopadhyay et al., 2014; Singh et al., 2016) with latest dyke activities (Kumar, Parashuramulu, Shankar, & Besse, 2017; Saha, 1994; Shankar, Srinivasa Sarma, Ramesh Babu, & Parashuramulu, 2018) similar to the event found in other parts of the world (Bleeker & Ernst, 2006; Harlan et al., 2003). Recently, Shankar et al. (2018) reported palaeopoles as an outcome of palaeomagnetic study on an accurately dated $1,765.3 \pm 1.0$ Ma dyke swarms (having WNW-ESE trends) from Singhbhum Craton. These dykes have profound implications for palaeogeographic reconstruction of India along with Baltica Craton and North China Craton. The study of Shankar et al. (2018) further indicates that the Baltica Craton and India linkage was stable for at least ~ 370 Ma (during 1,770 to 1,400 Ma). The presence of geometrically oriented Neoproterozoic mafic dyke-swarms in Singhbhum Craton (intruding the Palaeoproterozoic basement rocks) also serves as good assessor for reconstruction of LIP.

Kumar et al. (2017) on the basis of Pb–Pb baddeleyite ages and palaeomagnetic studies on a number of mafic dykes of Singhbhum Craton were of the opinion that both $2,762.4 \pm 2.0$ Ma and $2,752.0 \pm 0.9$ Ma ages of dyke activity correspond to similar mafic dykes of Pilbara Craton. A relatively older dyking-event at $2,783 \pm 1.2$ Ma from Singhbhum Craton is also well correlatable with that of Kaapvaal Craton. Documentation of Kumar et al. (2017) is very important in the sense that during Neoproterozoic time, Singhbhum Craton was proximal to Pilbara and Kaapvaal Craton and therefore they altogether could define the Vaalbara LIP. Role of Neoproterozoic crust-generation in the Singhbhum Craton has also been highlighted by Chaudhuri (2020) and this work also suggests a possible Pilbara connection of Singhbhum. The granite-greenstone belts containing banded iron formation (BIF) of the Gorumahisani-Badampahar-Daitari Iron Ore Group (IOG) comprises an integral part of the Archean granite

TABLE 1 Stratigraphy of the Singhbhum-Orissa Craton, Eastern India

Stratigraphic unit	Geological events	Major lithologies	Age (Ga)
Newer dolerite dykes and sills-phases I, II, and III	Intrusions of dykes and sills	Quartz dolerite	~ 2.0 – 1.0
Kolhan group	Deposition of sediments	Phyllite, limestone, sandstone-conglomerate	$\sim < 2.25$
Jagannathpur and Malangtoli lavas	Volcanic eruption	Basalts, basaltic andesites	~ 2.25
Dhanjori and Dalma volcanics, Tamperkola granites	Mafic volcanism and felsic plutonism	Ultramafic-mafic tuffs, basalts, quartzite-conglomerate High-Mg lavas, pyroclastic rocks, granite	~ 2.80
<i>Thermal metamorphism of OMG, OMTG, SBG-II and SBG-III</i>			3.07–3.05
Mayurbhanj granite and gabbro (MBG)	Coeval emplacement of MBG	Granite, gabbro, picrite, anorthosite	3.09
Simlipal lavas and metasediments	Formation of volcano-sedimentary basin	Spillites, tuffs, quartzites	$\sim > 3.09$
Singhbhum group	Formation and deformation of supracrustals sedimentation and magmatism	Pelites, felsic volcanic, mafic sills	~ 3.12 – 3.09
<i>Unconformity</i>			
<i>Thermal metamorphism of OMG due to SBG-III and Bonai granite emplacement</i>			~ 3.16 – 3.10
SBG-III	Emplacement of SBG-III	Granodiorite, granite	~ 3.12
Bonai granite	Plutonic emplacement	Granite, granodiorite	~ 3.16
Metamorphism of OMG, OMTG and IOG rocks			~ 3.24 – 3.20
Iron Ore Group (IOG)	Formation, structural deformation (folding) and metamorphism of IOG rocks	Mafic and felsic lavas, tuffs, shales, BHJ, BHQ, quartzite dolomite, conglomerate	~ 3.30 – 3.16
<i>Unconformity</i>			
<i>Thermal metamorphism of OMG and OMTG due to SBG-II and Nilgiri granite emplacement</i>			~ 3.30
Nilgiri granite	Emplacement of Nilgiri granite	Tonalite, granite	~ 3.29
SBG-II	Emplacement of SBG-II	Granodiorite	~ 3.33 – 3.30
Singhbhum granite (SBG-I)	Emplacement of granitoid plutons	Tonalite, granodiorite	~ 3.44 – ~ 3.38
Older Metamorphic Tonalite Gneiss (OMTG)	Folding of OMG supracrustals and synkinematic intrusion of tonalite	Tonalite gneiss, granodiorite	~ 3.44 – 3.42
Older Metamorphic Group (OMG)	Deposition of sediments with mafic volcanism and plutonism	Pelitic schists, banded calc-gneiss, amphibolites	~ 3.55 – 3.44
Unstable sialic crust		Sialic sediments	3.6– ~ 3.55

Note: After Misra (2006) and Saha, Ray, and Sarkar (1988).



INDEX	
	- Older Metamorphic Group (1)
	- Older Metamorphic Tonalite-gneiss (2)
	- Pala Lahara Gneiss (3)
	- Singhbhum Granite Phase I (4)
	- Singhbhum Granite Phase II and xenolith dominated areas of Bonai Granite (5)
	- Iron Ore Group lavas, ultramafics (7)
	- Iron Ore Group shales, tuffs, phyllites (8)
	- BHJ, BHQ and sandstone conglomerate of Iron Ore Group (9)
	- Singhbhum Granite Phase III; Bonai Granite; Chakradharpur Granite (10)
	- Dalma lavas (16)
	- Proterozoic Gabbro-anorthosite-ultramafics (17)
	- Kolhan Group and equivalents (18)
	- Soda granite, Arkasani Granite, Kulilpal Granite, alkaline granite (Beldih) (20)
	- Singhbhum Group pelites, psammipelites (11a)
	- Singhbhum Group pelites, mafic bodies (11b)
	- Singhbhum Group pelites, carbon phyllite (11c)
	- Singhbhum Group quartzites; Quartzites-pelites (12)
	- Dhanjori-Simplipal-Jagannathpur-Malangtoli lavas (15)
SSZ - Singhbhum Shear Zone	
CGC - Chhotanagpur Gneisses Complexes	

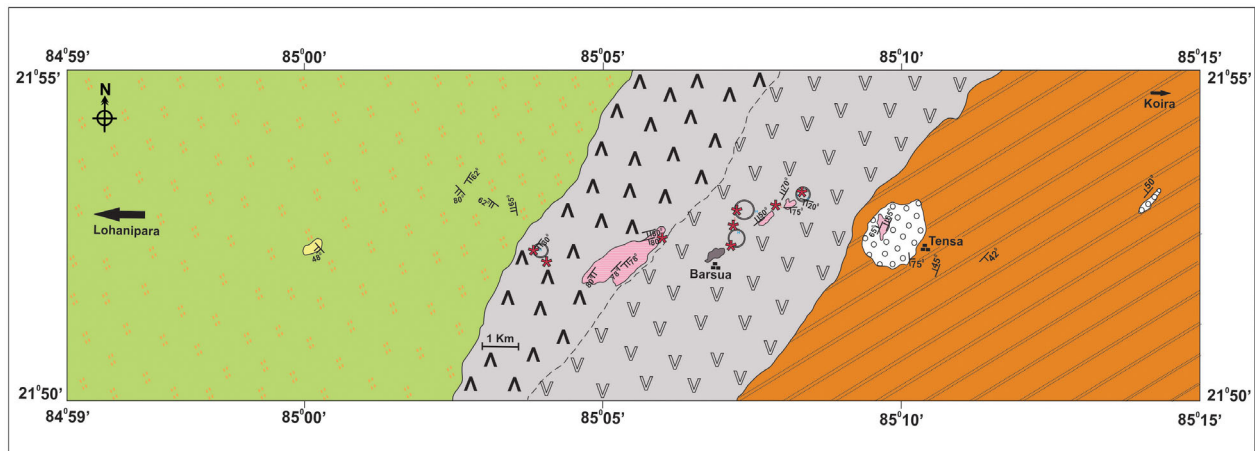
FIGURE 1 (a) Map showing different cratons in the peninsular India (Sharma, 2009). (b) Geological map of the Singhbhum North-Orissa region (after Saha, 1994). (c) Inset map showing enlarged portion of the study area marked by rectangular box [Colour figure can be viewed at wileyonlinelibrary.com]

greenstone terranes and Proterozoic supracrustals of the Singhbhum Craton (Manikyamba et al., 2015; Mohanty, 2012). The volcano-sedimentary sequences of IOG were deposited in Gorumahisani-Badampahar basin in the east, Noamundi-Jamda-Koira basin in the west, and Tomka-Daitari basin in the south of the Singhbhum Craton. These three IOG basins share similar lithostratigraphic successions marked by basal sandstones and conglomerates overlain by ferruginous shales, cherts, tuffs, tuffaceous shales, ultramafic-mafic-felsic volcanic rocks, and BIFs (Manikyamba et al., 2015; Misra, 2006; Mukhopadhyay, Ghosh, Zimmermann, Guha, & Mukherjee, 2012; Nelson, Bhattacharya, Thern, & Altermann, 2014; Saha, 1994). Sengupta, Acharyya, and Deshmeth (1997) studied geochemical characteristics of both eastern and western IOG. According to these authors, the main lithotypes for both the belts are dominantly metabasalts with minor presence of peridotitic komatiite and basaltic komatiite which typically occur in the eastern IOG basin. The authors are of the opinion that these basaltic rocks have been derived independently with no fractionation linkage with ultramafic rocks. Noting the geochemical character, Sengupta et al. (1997) have divided the basaltic rocks into three subtypes: (a) tholeiitic subtype mostly occurring within the eastern IOG basin, (b) calc-alkaline subtype typically present within western IOG basin, and (c) a transitional subtype whose geochemical signatures are intermediate between other two subtypes. Geochemical modelling indicates that the tholeiitic and calc-alkaline subtypes have different parentage controlled by variable degrees of mantle melting. A characteristic iron enrichment trend has been documented by Bose (2009) for the mafic lavas of

eastern IOG. The southern IOG basin shows three geochemically distinct lava types which are high Mg-type, moderate Mg-type, and low Mg-type which are corresponding to different parental magma (Bose, 2009; Saha, 1994). In a recent paper, Chaudhuri, Mazumder, and Arima (2015) have deciphered the presence of komatiites in some parts of eastern IOG basin (namely from Tua-Dungri sector). According to these authors, these komatiites are related to mantle plume activity in the Singhbhum Craton during the Mesoarchean. On the basis of detailed major, trace, and PGE studies, Singh et al. (2016) have elucidated presence of andesitic volcanism with calc-alkaline parentage in parts of western IOG basin. However, sustained geochemical work on volcanic rocks of western IOG basin are still lacking. In this view, this article presents new petrological and geochemical data for Precambrian mafic volcanic rocks from Koira sector of western IOG basin, Singhbhum Craton to (a) address the mantle processes and geodynamic conditions involved in their genesis and (b) constrain Archean ocean-continent convergent margin magmatism and crustal growth.

2 | GEOLOGICAL SETTING

The Indian Peninsular shield is an ensemble of differently evolved Archean-Palaeoproterozoic cratons overlain by Meso and Neoproterozoic platformal basins and penecontemporaneous to Proterozoic mobile belts with Archean signature (Mahadevan, 2008). Careful studies on these units are very helpful to understand Precambrian



INDEX






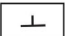


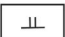



 - Banded Hematite Quartzite	 - Iron Ore Group Basalts (Flow II)	 - Location of High FeO-basalts (for Flow I & Flow II)
 - Conglomerate	 - Pyroclasts	 - Bedding Plane
 - Ferruginous Shale	 - Gabbro-Anorthosite	 - Cleavage Plane
 - Iron Ore Group Basalts (Flow I)	 - Quartzite	 - Location of the analyzed samples

FIGURE 2 Geological map of the study area. Sample locations of mafic volcanics from Flow I and Flow II (Iron Ore Group of rocks) have been marked with “*”. “○” indicates locations of high FeO pockets caused due to liquid immiscibility [Colour figure can be viewed at wileyonlinelibrary.com]

stratigraphic development (Saha & Mazumder, 2012). Mahadevan (2008) suggested that the styles of crustal growth in different parts of the Indian shield are markedly different wherein magmatism plays an important role that punctuated the continental evolution. The most ancient mafic magmatism within the cratonic nucleus is the main interest to understand the history of early growth of crust (Bose, 2009). The Singhbhum-North Orissa Craton of the eastern Indian shield is a Precambrian "granite greenstone terrain" (Mahadevan, 2002) and it

includes two major Precambrian crustal sub-provinces of the Indian shield namely the ancient Singhbhum-Orissa Iron Ore Craton (SOIOC) and the Proterozoic mobile belt which surrounds the craton in the west, north, and the east (Saha, 1994). The generalized geological succession of west Singhbhum area has been given by Saha (1994) (Table 1). The rocks of cratonic block range in age from ≥ 3.7 Ga to 1.0 Ga; however, majority of lithounits are >3.0 Ga (except some early Proterozoic supracrustal and Proterozoic igneous intrusive in the fringe and the

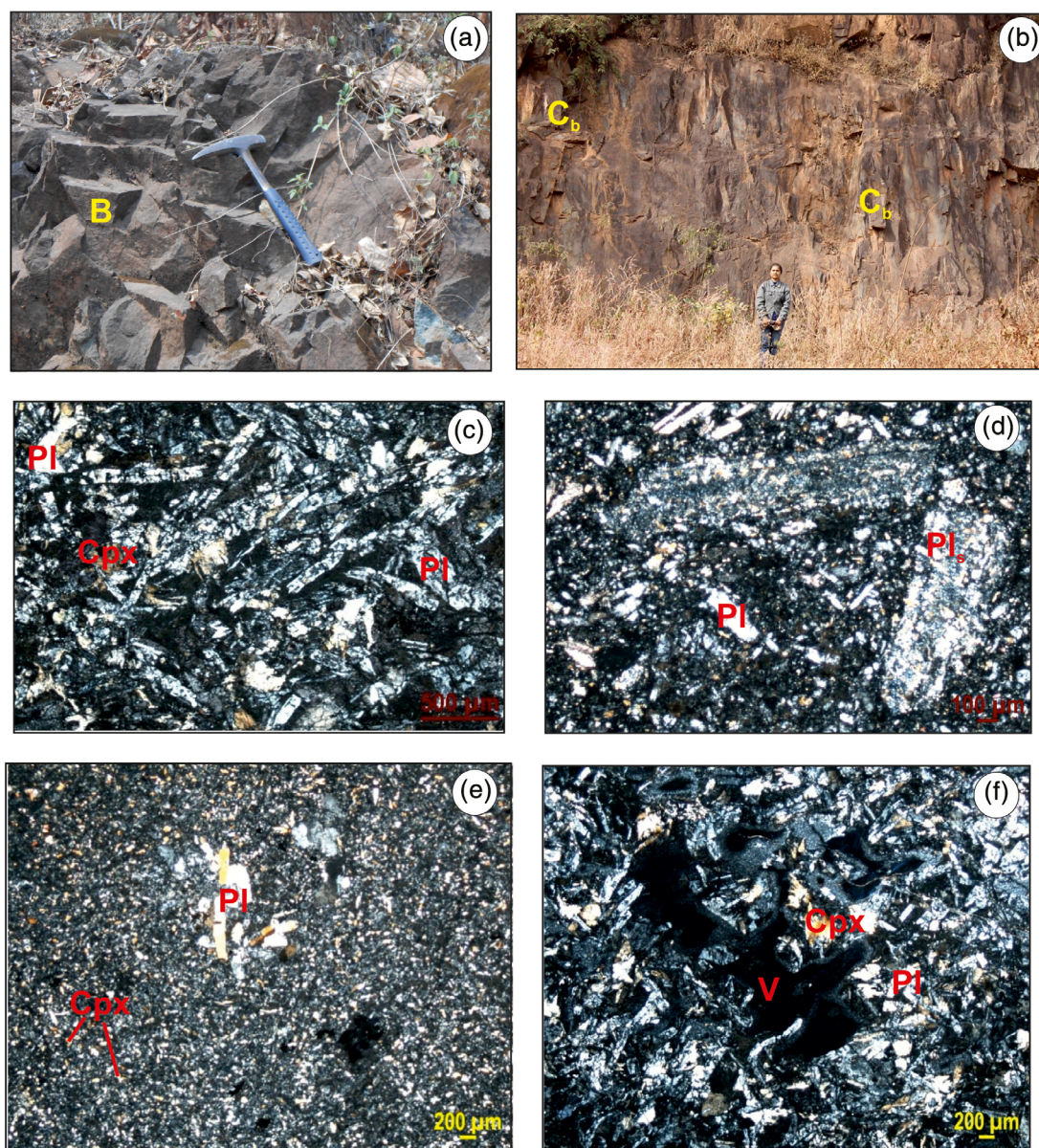


FIGURE 3 (a) Field photograph showing occurrence of mafic volcanics (IOG rocks), massive in nature with spaced joint (B - basalt). (b) Field photograph showing presence of well-exposed columnar basalt near Tensa (C_b - columnar basalt). The pattern of columnar structure is similar to that of Garibaldi Group of calc-alkaline volcanic rocks (Lawrence, Armstrong, & Berman, 1984). (c) Photomicrograph showing well-developed phenocrysts of plagioclase within finer groundmass (PI - plag, Cpx - clinopyroxene). (d) Photomicrograph showing highly saussuritized plagioclase phenocrysts embedded within finer grained groundmass (PI_s - saussuritized plag). (e) Photomicrograph showing aggregates of plagioclase phenocrysts showing glomeroporphyritic texture. Intergranular-intersertal textures are also seen (PI - plag, Cpx - clinopyroxene). (f) Photomicrograph showing occurrences of vug structure in glassy groundmass (PI - plag, Cpx - clinopyroxene, V - vug) [Colour figure can be viewed at wileyonlinelibrary.com]

TABLE 2 Major and trace element compositions of the IOG mafic volcanic rocks

	*810/1	*810/2	*814/1	*814/2	838/1	*838/2	*839/1	*839/2	812/1	812/2	812/3	812/4
SiO ₂	47.56	46.03	47.01	47.34	53.68	55.31	50.53	50.65	52.01	50.18	51.00	51.18
TiO ₂	2.50	2.39	1.41	1.40	1.12	1.55	1.47	1.43	1.24	1.15	1.19	1.18
Al ₂ O ₃	13.02	12.56	11.90	12.77	11.46	11.40	11.97	11.88	13.09	13.29	13.22	13.41
Fe ₂ O ₃	3.07	3.47	3.59	3.13	2.98	3.08	3.06	3.09	2.67	2.90	2.87	2.62
FeO	9.91	11.20	11.58	10.11	9.62	9.93	9.87	9.97	8.60	9.34	9.26	8.45
MnO	0.18	0.20	0.20	0.17	0.15	0.19	0.17	0.18	0.15	0.18	0.17	0.19
MgO	7.83	8.86	8.07	8.51	6.96	6.61	11.18	10.98	6.55	6.76	7.28	8.06
CaO	9.82	9.76	11.24	11.86	7.13	5.68	6.36	7.19	9.42	9.76	8.36	7.74
Na ₂ O	2.20	2.41	1.71	2.05	3.34	2.89	3.76	3.66	2.45	2.11	2.36	2.57
K ₂ O	1.16	0.31	0.44	0.55	0.87	0.66	0.20	0.31	1.13	1.59	1.51	1.58
P ₂ O ₅	0.23	0.25	0.15	0.15	0.13	0.18	0.12	0.13	0.20	0.19	0.19	0.19
LOI	3.85	2.74	5.57	5.19	2.43	2.56	3.06	2.57	2.60	3.27	2.31	2.82
Total	101.33	100.18	102.87	103.23	99.87	100.04	101.75	102.04	100.11	100.72	99.72	99.99
S.I.	32.40	33.75	31.78	34.95	29.28	28.53	39.83	39.20	30.61	29.78	31.27	34.62
D.I.	26.13	22.81	17.54	21.00	38.31	40.01	33.44	32.97	32.07	28.76	31.20	32.39
Na ₂ O + K ₂ O	3.36	2.72	2.15	2.60	4.21	3.55	3.96	3.97	3.58	3.70	3.87	4.15
FeO ^(t) /MgO	1.66	1.66	1.88	1.56	1.81	1.97	1.16	1.19	1.72	1.81	1.67	1.37
FeO ^(t)	12.98	14.67	15.17	13.24	12.60	13.01	12.93	13.06	11.27	12.24	12.13	11.07
SiO ₂ /Al ₂ O ₃	3.65	3.66	3.95	3.71	4.68	4.85	4.22	4.26	3.97	3.78	3.86	3.82
CaO/Al ₂ O ₃	0.75	0.78	0.94	0.93	0.62	0.50	0.53	0.61	0.72	0.73	0.63	0.58
Mg#	0.44	0.44	0.41	0.46	0.42	0.40	0.53	0.52	0.43	0.42	0.44	0.49
CIPW norm												
Q	-	-	-	-	4.03	10.93	-	-	3.96	0.80	1.54	0.40
Or	7.03	1.88	2.67	3.31	5.28	4.00	1.20	1.84	6.85	9.64	9.16	9.61
Ab	19.10	20.93	14.87	17.69	29.00	25.08	32.24	31.13	21.26	18.32	20.50	22.38
An	22.78	23.12	24.13	24.48	14.06	16.59	15.38	15.14	21.91	22.66	21.56	20.97
Diopside Wo	10.70	10.38	13.41	14.40	8.91	4.63	6.59	8.28	10.29	10.74	8.23	7.20
Diopside En	6.30	6.02	7.14	8.26	4.81	2.46	4.15	5.17	5.72	5.80	4.59	4.29
Diopside Fs	3.85	3.87	5.83	5.48	3.80	2.02	2.02	2.61	4.16	4.56	3.30	2.53
Hypersthene En	9.55	7.85	11.33	5.53	12.91	14.36	12.04	9.58	10.94	11.40	13.94	16.28
Hypersthene Fs	5.83	5.04	9.25	3.67	10.20	11.81	5.85	4.83	7.96	8.97	10.03	9.57
Olivine Fo	2.85	6.08	1.47	5.41	-	-	8.34	8.84	-	-	-	-
Olivine Fa	1.92	4.32	1.32	3.96	-	-	4.48	4.92	-	-	-	-
Mt	4.57	5.16	5.35	4.63	4.43	4.58	4.50	4.50	3.97	4.31	4.27	3.91
Il	4.87	4.66	2.75	2.71	2.18	3.02	2.83	2.73	2.42	2.24	2.32	2.31
Ap	0.52	0.56	0.34	0.33	0.29	0.40	0.27	0.29	0.45	0.43	0.43	0.43
Cr	36	38	58	61	22	17	45	48	27	27	29	30
Co	48	51	51	53	47	47	50	47	42	44	43	45
Ni	30	49	37	38	24	18	29	29	25	25	26	26
Rb	30	7	19	23	24	14	5	10	45	64	68	64
Sr	159	136	183	294	207	132	96	86	227	237	134	130
Cs	1.09	0.45	0.63	0.55	0.38	0.28	0.40	0.38	0.72	1.02	1.04	1.15
Ba	451	80	107	115	340	184	76	86	222	386	308	365
Ti	6,714	6,415	6,475	6,415	6,415	6,834	6,954	6,535	6,535	6,415	6,654	6,475
K	9,630	2,573	3,653	4,566	7,222	5,479	1,660	2,573	9,381	13,200	12,535	13,117
Sc	28.6	28.6	22.0	23.4	25.9	24.6	23.0	23.8	28.9	28.0	27.4	28.1

(Continues)

TABLE 2 (Continued)

	*810/1	*810/2	*814/1	*814/2	838/1	*838/2	*839/1	*839/2	812/1	812/2	812/3	812/4
V	316	334	42	45	40	57	41	43	268	206	204	235
Ta	1.4	1.3	0.4	0.4	0.5	0.8	0.5	0.5	3.0	3.2	3.1	2.5
Nb	13.3	13.1	6.9	7.0	7.7	11.3	7.9	7.9	29.7	29.8	29.6	28.6
Zr	218.4	212.4	126.0	134.2	145.1	207.3	160.0	151.9	382.1	323.5	314.7	357.1
Hf	4.8	4.5	3.8	3.9	4.3	6.1	4.8	4.6	7.1	6.9	6.7	6.9
Th	1.5	1.5	1.8	1.7	3.8	5.7	3.1	3.0	6.6	6.5	6.4	6.5
U	0.30	0.33	1.08	1.17	2.30	2.87	1.25	1.31	1.00	0.90	0.95	0.92
Y	42.5	42.3	32.4	33.6	30.0	38.9	33.9	34.4	54.7	51.4	53.6	54.2
La	16.76	16.87	12.50	13.86	21.53	32.53	17.59	16.04	39.82	39.36	39.16	42.43
Ce	39.35	39.31	29.09	31.61	45.02	66.14	38.75	36.11	81.45	81.29	79.88	86.61
Pr	4.30	4.27	3.66	4.02	5.14	7.47	4.69	4.37	7.59	7.58	7.45	8.06
Nd	24.03	24.15	16.92	18.48	20.87	30.56	19.77	19.30	36.92	36.72	36.50	38.55
Sm	5.42	5.41	4.16	4.46	4.56	6.36	4.69	4.57	7.04	7.01	6.99	7.27
Eu	1.98	1.91	0.78	0.83	0.61	0.88	0.75	0.69	1.69	1.70	1.52	1.72
Gd	6.96	6.95	3.88	4.00	3.66	5.17	4.13	4.09	8.60	8.45	8.40	8.51
Tb	1.16	1.16	0.68	0.72	0.62	0.87	0.75	0.73	1.47	1.43	1.41	1.48
Dy	6.41	6.56	4.95	5.18	4.54	6.45	5.44	5.36	8.34	7.94	7.98	8.15
Ho	1.39	1.40	0.60	0.63	0.54	0.75	0.67	0.66	1.78	1.69	1.74	1.78
Er	4.46	4.42	1.97	2.09	1.89	2.48	2.21	2.28	5.88	5.63	5.75	5.83
Tm	0.73	0.73	0.29	0.28	0.26	0.35	0.30	0.33	0.96	0.93	0.96	0.98
Yb	3.95	3.94	2.85	2.82	2.55	3.42	3.05	3.08	5.20	5.07	5.04	5.20
Lu	0.61	0.61	0.48	0.47	0.45	0.56	0.52	0.52	0.78	0.75	0.76	0.80
∑REE	117.51	117.67	82.80	89.46	112.25	164.00	103.31	98.12	207.52	205.57	203.55	217.36
Cu	151	144	1	1	1	1	0	0	116	116	118	108
Zn	104	133	81	76	52	31	27	29	108	103	94	91
Ga	18.2	19.6	16.7	18.4	15.1	16.9	15.7	15.5	19.1	20.1	19.0	19.8
Ni/Co	0.63	0.96	0.73	0.72	0.51	0.38	0.57	0.62	0.61	0.57	0.60	0.59
Ce/Yb	9.97	9.99	10.21	11.21	17.63	19.32	12.69	11.74	15.65	16.04	15.85	16.64
Th/Yb	0.39	0.39	0.62	0.61	1.49	1.65	1.02	0.98	1.27	1.28	1.26	1.24
Ti/Zr	30.75	30.21	51.40	47.81	44.21	32.97	43.47	43.02	17.10	19.83	21.15	18.13
Zr/Y	5.13	5.02	3.89	4.00	4.84	5.33	4.73	4.42	6.98	6.29	5.87	6.59
Nb/Y	0.31	0.31	0.21	0.21	0.26	0.29	0.23	0.23	0.54	0.58	0.55	0.53
V/Cr	8.74	8.76	0.73	0.75	1.78	3.23	0.91	0.90	9.95	7.52	7.05	7.96
Nb/Yb	3.38	3.32	2.43	2.49	3.00	3.31	2.60	2.57	5.72	5.87	5.87	5.50
(Gd/Yb) _N	1.46	1.46	1.13	1.17	1.19	1.25	1.12	1.10	1.37	1.38	1.38	1.35
(La/Yb) _N	3.05	3.07	3.15	3.52	6.05	6.81	4.13	3.74	5.49	5.57	5.57	5.85
(Ce/Yb) _N	2.77	2.77	2.83	3.11	4.90	5.37	3.53	3.26	4.35	4.45	4.40	4.62
(Sm/Yb) _{PM}	1.53	1.53	1.62	1.76	1.98	2.06	1.71	1.65	1.50	1.53	1.54	1.55
(La/Sm) _N	2.00	2.01	1.94	2.01	3.05	3.30	2.42	2.27	3.65	3.62	3.62	3.77
(Sm/Yb) _N	1.52	1.53	1.62	1.76	1.99	2.07	1.71	1.65	1.50	1.54	1.54	1.55
Nb/U	45.10	39.36	6.44	5.99	3.33	3.95	6.37	6.02	29.89	32.93	31.21	31.14
La/Yb	4.25	4.29	4.39	4.91	8.43	9.50	5.76	5.21	7.65	7.77	7.77	8.15
Th/Ta	1.11	1.16	4.23	4.14	8.08	7.46	5.95	5.67	2.17	2.05	2.06	2.63
Zr/Nb	16.37	16.23	18.16	19.10	18.95	18.31	20.16	19.23	12.85	10.86	10.64	12.49
Nb/Th	8.66	8.51	3.93	4.09	2.01	2.00	2.56	2.62	4.52	4.57	4.66	4.42
La/Nb	1.26	1.29	1.80	1.97	2.81	2.87	2.22	2.03	1.34	1.32	1.32	1.48

TABLE 2 (Continued)

	*810/1	*810/2	*814/1	*814/2	838/1	*838/2	*839/1	*839/2	812/1	812/2	812/3	812/4
Ba/Nb	33.85	6.13	15.39	16.34	44.40	16.26	9.52	10.89	7.45	12.96	10.41	12.76
Ba/Th	293.20	52.13	60.45	66.86	89.25	32.55	24.36	28.48	33.65	59.23	48.49	56.37
Rb/Nb	2.25	0.50	2.67	3.26	3.15	1.23	0.60	1.23	1.51	2.15	2.30	2.22
K/Nb	722.05	196.70	526.68	650.08	943.44	483.98	209.26	325.81	315.39	443.27	423.86	458.59
Th/La	0.09	0.09	0.14	0.12	0.18	0.17	0.18	0.19	0.17	0.17	0.16	0.15
Ba/La	26.93	4.75	8.54	8.28	15.79	5.66	4.30	5.36	5.56	9.80	7.87	8.60
Th/Nb	0.12	0.12	0.25	0.24	0.50	0.50	0.39	0.38	0.22	0.22	0.21	0.23
Sr/Y	3.73	3.21	5.67	8.77	6.89	3.40	2.84	2.51	4.16	4.61	2.51	2.41
Nb/La	0.80	0.78	0.55	0.51	0.36	0.35	0.45	0.49	0.75	0.76	0.76	0.67
(Nb/Th) _{PM}	1.03	1.01	0.47	0.49	0.24	0.24	0.30	0.31	0.54	0.55	0.56	0.53
(Nb/La) _{PM}	0.77	0.75	0.53	0.49	0.34	0.34	0.43	0.47	0.72	0.73	0.73	0.65
Th/Ce	0.04	0.04	0.06	0.05	0.08	0.09	0.08	0.08	0.08	0.08	0.08	0.07
Sc/Yb	7.24	7.26	7.73	8.29	10.13	7.19	7.53	7.75	5.55	5.52	5.44	5.40
	812/5	836/1	836/2	836/3	*845/1	840/1	840/2					
SiO ₂	52.29	46.64	50.11	50.14	54.64	51.43	51.27					
TiO ₂	1.16	1.23	1.28	1.27	1.56	1.35	1.46					
Al ₂ O ₃	12.98	11.30	12.09	13.33	11.35	12.85	12.59					
Fe ₂ O ₃	2.80	2.74	2.80	2.81	3.32	2.65	2.78					
FeO	9.02	8.83	9.04	9.07	10.70	8.55	8.97					
MnO	0.16	0.15	0.20	0.18	0.16	0.16	0.16					
MgO	6.77	8.94	9.31	9.47	5.38	8.82	6.64					
CaO	8.71	15.61	9.95	8.58	6.70	8.60	8.94					
Na ₂ O	2.34	1.50	2.48	2.66	2.16	3.03	2.62					
K ₂ O	1.53	0.21	1.29	1.07	1.25	1.42	1.96					
P ₂ O ₅	0.19	0.13	0.13	0.11	0.15	0.17	0.23					
LOI	2.93	2.11	3.02	2.62	2.64	2.95	2.01					
Total	100.88	99.39	101.70	101.31	100.01	101.98	99.63					
S.I.	30.14	40.23	37.36	37.76	23.59	36.04	28.91					
D.I.	33.03	14.33	28.98	29.22	38.53	34.36	34.83					
Na ₂ O + K ₂ O	3.87	1.71	3.77	3.73	3.41	4.45	4.58					
FeO ^(t) /MgO	1.75	1.29	1.27	1.25	2.61	1.27	1.77					
FeO ^(t)	11.82	11.57	11.84	11.88	14.02	11.20	11.75					
SiO ₂ /Al ₂ O ₃	4.03	4.13	4.14	3.76	4.81	4.00	4.07					
CaO/Al ₂ O ₃	0.67	1.38	0.82	0.64	0.59	0.67	0.71					
Mg#	0.43	0.50	0.51	0.51	0.33	0.51	0.43					
CIPW norm												
Q	3.59	-	-	-	12.17	-	0.26					
Or	9.23	1.28	7.72	6.41	7.59	8.47	11.86					
Ab	20.21	13.05	21.26	22.81	18.77	25.89	22.71					
An	20.81	24.12	18.27	21.54	18.04	17.42	17.20					
Diopside Wo	9.19	22.77	12.88	8.70	6.29	10.23	11.13					
Diopside En	5.05	13.85	7.86	5.34	2.96	6.30	6.17					
Diopside Fs	3.80	7.62	4.27	2.86	3.25	3.33	4.52					
Hypersthene En	12.10	0.78	7.86	11.52	10.74	9.20	10.70					
Hypersthene Fs	9.10	0.43	4.27	6.16	11.78	4.87	7.84					
Olivine Fo	-	5.71	5.37	4.86	-	4.62	-					

(Continues)

TABLE 2 (Continued)

	812/5	836/1	836/2	836/3	*845/1	840/1	840/2
Olivine Fa	-	3.47	3.22	2.87	-	2.70	-
Mt	4.14	4.08	4.11	4.13	4.94	3.88	4.13
Il	2.25	2.40	2.46	2.44	3.04	2.59	2.84
Ap	0.42	0.29	0.29	0.24	0.34	0.37	0.51
Cr	27	55	48	46	48	23	18
Co	44	49	49	44	46	44	44
Ni	25	43	34	100	28	20	18
Rb	69	5	40	42	31	47	61
Sr	224	968	135	119	230	118	177
Cs	0.97	0.26	0.66	0.64	1.46	0.45	0.42
Ba	290	89	563	189	312	416	608
Ti	6,595	6,535	6,355	6,415	6,115	5,036	5,096
K	12,701	1,743	10,709	8,883	10,377	11,788	16,271
Sc	27.9	23.0	22.4	18.9	25.7	23.3	25.2
V	244	46	42	36	225	39	43
Ta	2.5	0.5	0.5	0.4	1.4	0.9	1.3
Nb	28.3	7.9	7.7	6.7	7.2	17.8	24.4
Zr	314.5	160.9	151.7	126.2	227.6	245.6	319.8
Hf	6.7	5.0	4.5	3.9	4.7	6.3	8.6
Th	6.3	3.0	2.8	2.5	3.7	5.3	7.4
U	0.99	1.79	1.76	2.22	1.10	1.58	2.38
Y	53.2	35.5	33.5	29.0	35.0	42.3	54.8
La	39.93	18.81	18.58	14.98	23.62	31.09	43.05
Ce	80.40	40.48	40.16	33.13	53.13	66.04	88.59
Pr	7.52	4.80	4.68	4.09	4.88	7.40	9.82
Nd	36.52	20.88	20.42	17.09	24.26	30.18	38.91
Sm	6.97	4.84	4.66	4.12	5.14	6.08	7.80
Eu	1.68	0.92	0.66	0.59	1.47	0.83	0.97
Gd	8.32	4.29	4.03	3.51	5.46	5.14	6.72
Tb	1.42	0.76	0.70	0.60	0.92	0.86	1.15
Dy	8.00	5.67	5.06	4.51	4.99	6.41	8.48
Ho	1.74	0.69	0.62	0.54	1.04	0.77	1.04
Er	5.67	2.29	2.11	1.91	3.35	2.63	3.50
Tm	0.95	0.32	0.31	0.27	0.57	0.36	0.50
Yb	5.17	3.20	3.07	2.75	3.14	3.70	5.05
Lu	0.79	0.54	0.51	0.47	0.50	0.60	0.80
Σ REE	205.08	108.49	105.55	88.56	132.47	162.11	216.38
Cu	118	1	1	1	117	1	1
Zn	85	43	148	35	150	25	27
Ga	19.2	27.0	15.0	13.9	21.8	18.1	18.7
Ni/Co	0.58	0.87	0.69	2.29	0.61	0.46	0.41
Ce/Yb	15.54	12.63	13.08	12.04	16.90	17.83	17.53
Th/Yb	1.22	0.95	0.91	0.91	1.17	1.44	1.47
Ti/Zr	20.97	40.61	41.89	50.84	26.87	20.50	15.93
Zr/Y	5.91	4.53	4.53	4.35	6.50	5.81	5.83
Nb/Y	0.53	0.22	0.23	0.23	0.21	0.42	0.45

TABLE 2 (Continued)

	812/5	836/1	836/2	836/3	*845/1	840/1	840/2
V/Cr	8.91	0.84	0.88	0.79	4.71	1.68	2.39
Nb/Yb	5.47	2.48	2.51	2.45	2.29	4.80	4.84
(Gd/Yb) _N	1.33	1.11	1.08	1.05	1.44	1.15	1.10
(La/Yb) _N	5.54	4.21	4.34	3.91	5.39	6.02	6.11
(Ce/Yb) _N	4.32	3.51	3.63	3.35	4.69	4.95	4.87
(Sm/Yb) _{PM}	1.50	1.68	1.68	1.66	1.81	1.82	1.71
(La/Sm) _N	3.70	2.51	2.57	2.35	2.97	3.30	3.56
(Sm/Yb) _N	1.50	1.68	1.69	1.66	1.82	1.83	1.72
Nb/U	28.54	4.44	4.37	3.03	6.54	11.25	10.27
La/Yb	7.72	5.87	6.05	5.45	7.51	8.39	8.52
Th/Ta	2.55	5.79	5.44	5.88	2.57	5.86	5.87
Zr/Nb	11.12	20.24	19.70	18.76	31.54	13.83	13.09
Nb/Th	4.49	2.62	2.75	2.68	1.95	3.34	3.28
La/Nb	1.41	2.37	2.41	2.23	3.27	1.75	1.76
Ba/Nb	10.25	11.23	73.10	28.07	43.20	23.41	24.88
Ba/Th	46.01	29.41	200.80	75.15	84.37	78.20	81.66
Rb/Nb	2.42	0.62	5.26	6.29	4.34	2.63	2.51
K/Nb	449.09	219.35	1,390.22	1,320.82	1,438.23	663.58	665.93
Th/La	0.16	0.16	0.15	0.17	0.16	0.17	0.17
Ba/La	7.26	4.74	30.31	12.60	13.20	13.37	14.12
Th/Nb	0.22	0.38	0.36	0.37	0.51	0.30	0.30
Sr/Y	4.21	27.28	4.04	4.11	6.57	2.79	3.23
Nb/La	0.71	0.42	0.41	0.45	0.31	0.57	0.57
(Nb/Th) _{PM}	0.54	0.31	0.33	0.32	0.23	0.40	0.39
(Nb/La) _{PM}	0.68	0.41	0.40	0.43	0.29	0.55	0.55
Th/Ce	0.08	0.07	0.07	0.08	0.07	0.08	0.08
Sc/Yb	5.40	7.17	7.29	6.87	8.18	6.29	4.99

Note: * indicates high FeO sub type (having FeO^t > 12.60 wt%). Other samples belong to low FeO sub type (having FeO^t < 12.60 wt%).

Newer Dolerite Dyke Swarms). These rocks can be divided into two major groups of supracrustals: (a) the Older Metamorphic Group (OMG), and (b) the IOG supracrustal (Saha, 1994).

The central portion of the craton mostly occupied by Palaeoarchean granitoids of different phases (Misra et al., 1999; Nelson et al., 2014; Tait et al., 2011; Upadhyay, Chattopadhyay, Kooijman, Mezger, & Berndt, 2014). The low-medium grade (greenschist-amphibolite facies) metamorphic basement of Archean age comprises tonalite-trondhjemite-granodiorite (TTG) gneisses (~3.53–3.29 Ga) termed as Older Metamorphic Tonalite Gneiss (OMTG) and 12 several granitic plutons together known as Singhbhum Granite (SG) with oldest supracrustal enclaves, OMG of rocks (Dey, Topno, Liu, & Zong, 2017; Sreenivas et al., 2019). The largest exposure of OMTG is located in the western part of Singhbhum Craton, near Champua. Recent U–Pb dates indicate multi-phased styles of OMTG which includes ~3.8, ~3.53, ~3.44, and 3.33–~3.32 Ga granitoids (Acharyya, Gupta, & Orihashi, 2010; Dey et al., 2017; Nelson

et al., 2014; Sengupta, Corfu, McNutt, & Paul, 1996; Upadhyay et al., 2014). Recent field studies and U–Pb age determination indicate that OMTG is occurred as basement rocks to OMG-sediments (Dey et al., 2017; Nelson et al., 2014; Roy & Bhattacharya, 2012; Saha, Hofmann, & Xie, 2012). Similar evidence of having felsic basement rocks in this craton has been provided by Ghosh, Vermeesch, Gain, and Mondal (2019). Moreover, evidence of Eoarchean magmatism in Singhbhum Craton (recorded by magmatic zircon age of 3.505 Ga) has been advocated by Sreenivas et al. (2019). According to these authors, the Eoarchean detrital zircons in this terrane manifest crustal component that has been generated by recycling of Hadean felsic lithology formed at ~4.3–4.2 Ga (Chaudhuri, Wan, Mazumder, Ma, & Dunyi Liu, 2018) and ~3.95 Ga. The SG is surrounded by Palaeoarchean volcano-sedimentary rocks known as IOG distributed in three different prominent basins (Jamda-Koira, Tomka-Daitari, and Gorumahisani-Badampahar) (Acharyya, 1993; Dey et al., 2017; Mazumder et al., 2012; Mukhopadhyay et al., 2012; Saha, 1994;

Sengupta et al., 1997). There is a general consensus that in this region, continental crust- building process initiated during Hadean-Eoarchean time and the rocks were subsequently recycled to generate Palaeoarchean and younger crust (Mukhopadhyay & Matin, 2020).

The IOG constitutes the major supracrustal unit in the Singhbhum-Orissa Iron Ore Craton (SOIOC) and it is composed of low-grade meta-sediments, including phyllites, tuffaceous shales, banded haematite jasper (BHJ) with Iron ore, ferruginous quartzite, local dolomite, acid-intermediate, and mafic volcanics with mafic sill like intrusive. The ultramafic-mafic volcanism with deposition of sedimentary sequences with BIF representing the IOG supracrustals is analogous with platform greenstone belt sequences and indicate second cycle of volcanism and sedimentation in the Singhbhum Craton (Condie, 1990; De Wit & Ashwal, 1995; Thurston, 1990). The age of sedimentation for the IOG has been interpreted to be in the range of 3.3–3.1 Ga (Saha et al., 1988). The type area of the IOG (c.3,100 Ma; Saha et al., 1988)

lies in the Noamundi-Jamda-Koira valley in the southern part of western IOG basin (trending NNE–SSW). Earlier workers suggested a synclinorium structure for the western IOG which was confirmed subsequently on the basis of tectonic analysis endorsing to a regional structure of synclinorium overturned towards the southeast (Jones, 1934; Sarkar & Saha, 1962, 1963). Mukhopadhyay et al. (2008) documented $3,506.8 \pm 2.3$ Ma U–Pb SHRIMP Zircon age for dacitic lava from the southern IOG. Stratabound magnetite deposits from the IOG have also been recorded by some workers (Mukhopadhyay, Gutzmer, Beukes, & Hayashi, 2008). The western part of IOG can be best studied in Koira-Noamundi-Champua area and Chaibasa-Saraikela-Chakradharpur area (Saha, 1994) (Figure 1). U–Pb zircon age (3.4 Ga) has been reported for the IOG volcanic rocks of Noamundi–Koira valley (Mukhopadhyay, Gutzmer, et al., 2008). Further, an age of ~ 3.39 Ga (from U–Pb LA-ICP-MS zircons) was documented from acid tuffs of western IOG basin by Basu, Bandyopadhyay, Chakraborti, and

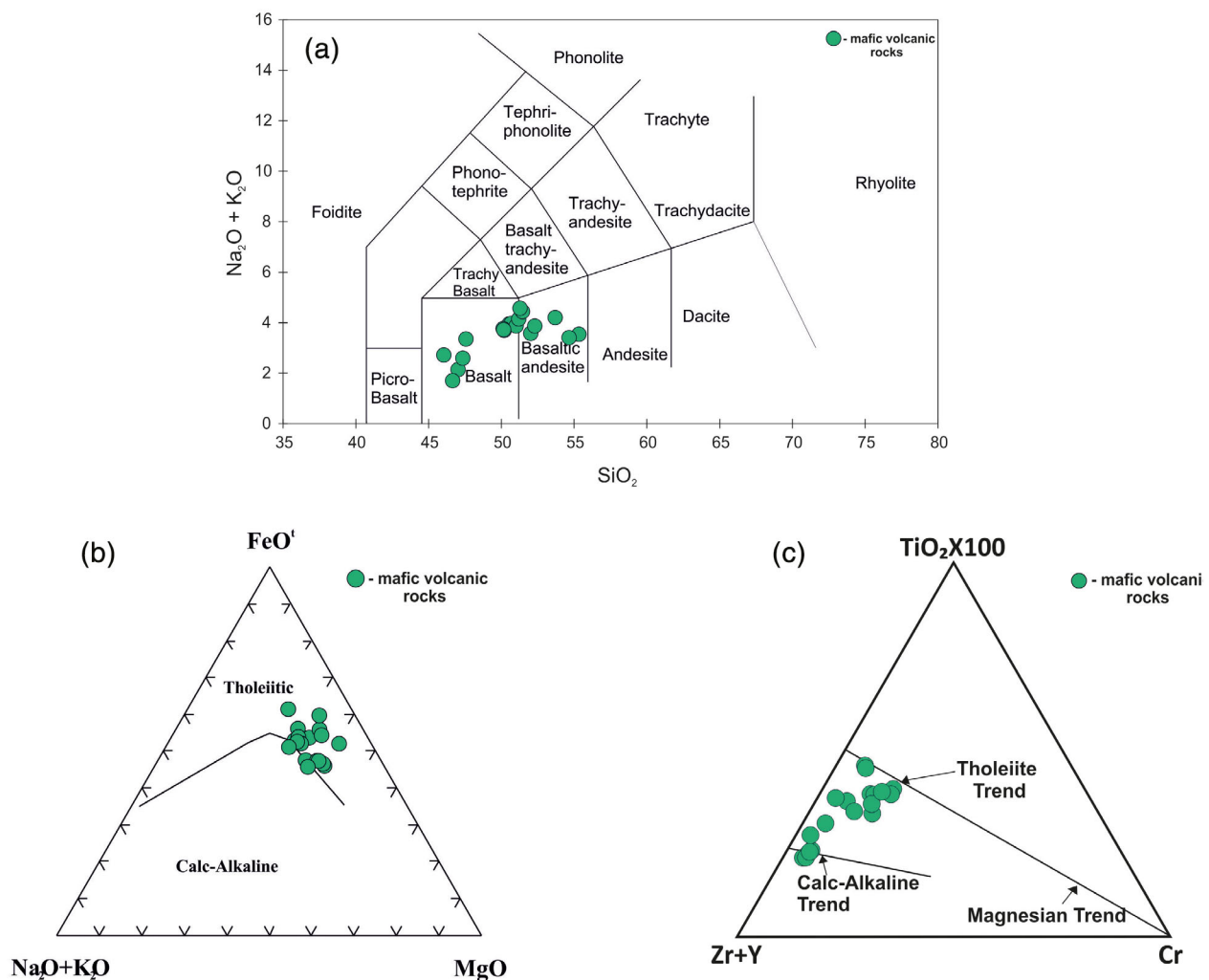


FIGURE 4 (a) Total alkali ($\text{Na}_2\text{O} + \text{K}_2\text{O}$) vs. silica (SiO_2) diagram (after Le Bas, Le Maitre, Streckeisen, & Zanettin, 1986). The mafic volcanic samples fall in the fields of basalt and basaltic andesite. (b) AFM (Total alkali- FeO^T - MgO) diagram (after Irvine & Baragar, 1971) showing a tholeiitic trend or marks a transition between tholeiitic and calc-alkaline character. (c) Y ($\text{Zr} + \text{Y}$) – T ($\text{TiO}_2 \times 100$) – C (Cr) diagram (after Davies, Grant, & Whitehead, 1979) showing transitional character between tholeiite and calc-alkaline trend with a minor spill over calc-alkaline trend [Colour figure can be viewed at wileyonlinelibrary.com]

Zou (2008). The age data for eastern IOG basin is scanty and there is no direct age-documentation from this belt. However, a minimum age of 3.1 Ga can be inferred from a granite body intrusive into this belt (Saha, 1994). The deformation, metamorphism, and migmatization of the Iron ore orogeny at 3.35–3.3 Ga overprinted the older sequences of the Singhbhum Craton and were followed by rifting and

emplacement of mafic dykes. Recent studies by Srivastava, Söderlund, Ernst, Mondal, & Samal (2016) and Kumar et al. (2017) demonstrate that the mafic dyke intrusions occurring in the Singhbhum Craton correspond to discrete age ranges which are ~ 2.8 Ga, ~ 2.7 – 2.6 Ga, ~ 2.25 Ga, and ~ 1.77 – 1.76 Ma. Earlier work by Bose (2009) suggests that IOG of rocks occurring in different basins are stratigraphically equivalent and their variable structural frameworks correspond to different tectonic styles. In recent years, it has convincingly been shown that some parts of IOG has sufficiently older history (Palaeoarchean) as documented by 3.505 Ga age (U–Pb) of constituent zircon from dacitic rocks (Sreenivas et al., 2019).

The present study areas include Koira ($21^{\circ}54'29.4''N; 85^{\circ}15'11.3''E$), Tensa ($21^{\circ}52'13.4''N; 85^{\circ}10'18.0''E$), and Barsua ($21^{\circ}52'12.4''N; 85^{\circ}06'45.0''E$) areas which constitute a part of western IOG

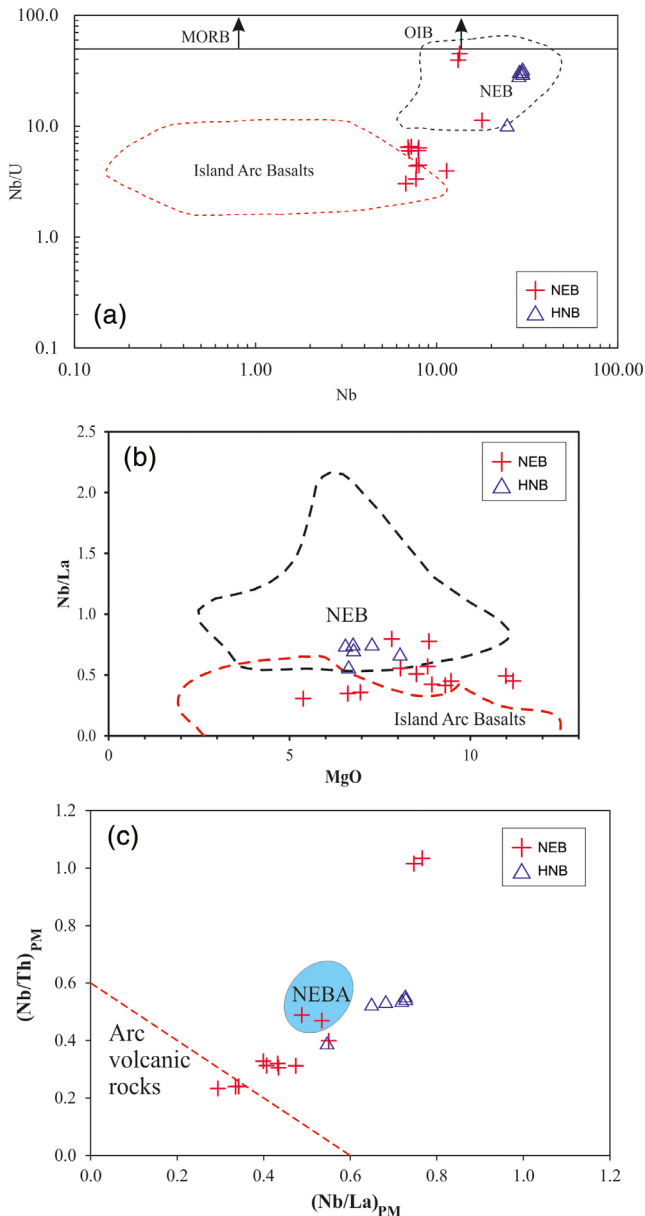


FIGURE 5 (a) Nb/U vs. Nb relationship (after Kepezhinkas, Defant, & Drummond, 1996) showing moderate and high Nb contents of Nb-enriched basalts (NEB) and high-Nb basalts (HNB) and their resemblance with the Phanerozoic counterparts. (b) Nb/La vs. MgO diagram (after Kepezhinkas et al., 1996) in which NEBs and HNBs are plotting in the field of Nb-enriched basalts. (c) $(Nb/Th)_{PM}$ vs. $(Nb/La)_{PM}$ diagram in which the samples are falling in the field of Phanerozoic NEBA (Kepezhinkas et al., 1997; Sajona, Maury, Bellon, Cotton, & Defant, 1996). Dashed line demarcates high ratios of NEB field from the arc basalts and andesites (after Polat & Kerrich, 2001) [Colour figure can be viewed at wileyonlinelibrary.com]

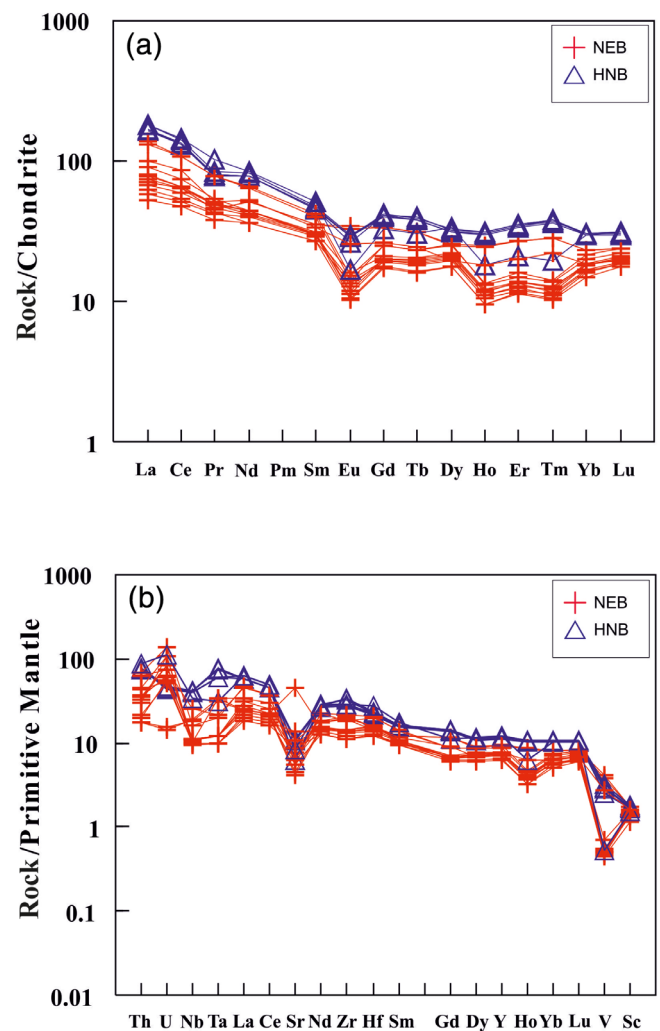


FIGURE 6 (a) Chondrite-normalized rare earth element (REE) patterns for NEB and HNB of studied area exhibit uniform LREE enrichment with distinct Eu negative anomalies. Normalization factors after Sun and McDonough (1989). (b) Primitive mantle-normalized incompatible trace element patterns for NEB and HNB reflect enrichment in LILE and LREE with prominent Nb-Ta anomalies. Normalization factors after Sun and McDonough (1989) [Colour figure can be viewed at wileyonlinelibrary.com]

basin of Singhbhum Craton. The predominant lithological associations comprise mafic volcanic rocks, ferruginous shales, banded

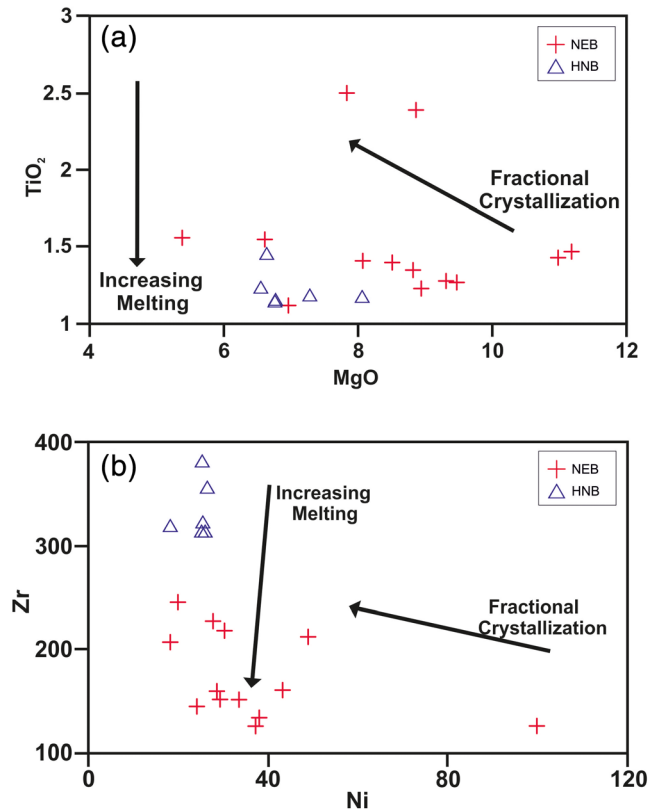


FIGURE 7 (a) TiO₂ vs. MgO diagram (after Condie, 2001) showing pronounced effect of fractional crystallization with the effects of continued melting; (b) Plots of Zr vs. Ni (after Condie, 2001) for the studied samples which displays a fractional crystallization trend [Colour figure can be viewed at [wileyonlinelibrary.com](https://onlinelibrary.com)]

haematite quartzite, polymictic conglomerate, quartzite xenolith, pyroclasts, and gabbro-anorthosites (Figure 2). The Banded Haematite Quartzite rock unit develops alternate crude bandings made up of haematite and quartzite. Well-developed compositional layering is observed in the ferruginous shale. Polymictic conglomerate comprises pebbles of different types (namely, quartz, feldspar, and haematite) having variable size-ranges. The mafic volcanic rocks are located at and around Barsua-Tensa region are predominantly massive with the presence of cleavage at some places (Figure 3a). These rocks show an overall NE-SW trend with moderate dip towards NW direction (Figure 2). Based on field observations, two distinct lava flows (Flow-I: older and Flow-II: younger) have been identified along with a small pyroclast band within Flow I (Figure 2) and well-developed columnar jointing at some places (Figure 3b). Some of the volcanic rocks show amygdaloidal structure with secondary vesicular fillings. Coarse-grained gabbro rocks (with both melano- and leuco- varieties) show prominent igneous layering and are well exposed in the study area. Saha (1994) opined that these bodies are of Proterozoic age but recent studies by Manikyamba et al. (2020) indicate their Mesoproterozoic age.

3 | SAMPLING AND ANALYTICAL TECHNIQUES

Sampling was carried out in and around Tensa-Barsua, Singhbhum Craton. Fresh and relatively unaltered samples were collected in the field from representative zones of two lava flows. After detailed petrographic studies, 19 samples of volcanic rocks from study area were selected for whole rock analysis (major, trace, and rare earth element concentrations) at CSIR-National Geophysical Research

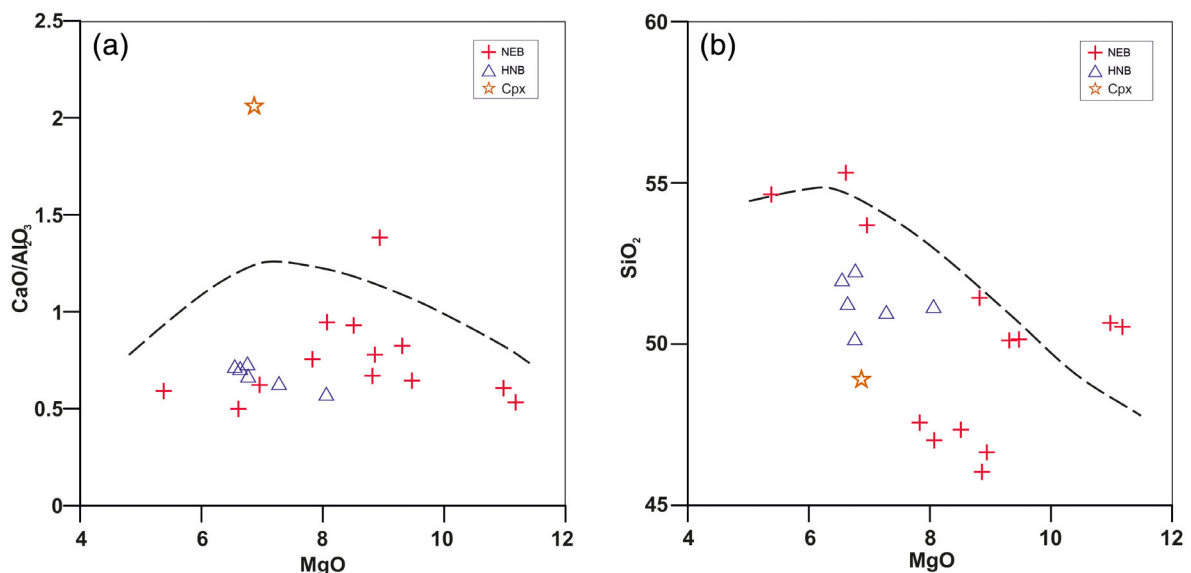


FIGURE 8 (a and b) Variations of different major oxides and their respective ratios with respect to MgO for the analysed samples. "★" indicates clinopyroxene composition taken from Cox et al. (1979) [Colour figure can be viewed at [wileyonlinelibrary.com](https://onlinelibrary.com)]

Institute, India. Major elements were analysed by XRF (Phillips MAGIX PRO Model 2440) using pressed pellets following the method of Krishna, Murthy, & Govil (2007). Trace elements (including REE) were determined by Inductively Coupled Plasma Mass Spectrometry (ICP-MS; Perkin Elmer SCIEX ELAN DRC II) and high resolution inductively coupled mass spectrometer (HR-ICP-MS) (Nu Instruments Attom, UK). The analytical procedure, precision, and accuracy for ICP-MS and HR-ICP-MS are given in Manikyamba, Kerrich, Khanna, Satyanarayanan, & Krishna (2009) and Manikyamba et al. (2014). BHVO-1 and JB-2 were run as standard reference materials during the analysis and ^{103}Rh was used as an internal standard and external drift was corrected by repeated analyses of standards which were also used as calibration standards

accordingly. Precision and reproducibility obtained for international reference materials are given in Supplementary Table 1 that are found to be better than 2% RSD for majority of the trace elements.

4 | PETROGRAPHY

The IOG mafic volcanic rocks are composed of plagioclase, clinopyroxene, and opaque minerals (ilmenite). Phenocryst is mainly made up of plagioclase grain (Figure 3c) which are saussuritized at places (Figure 3d). The groundmass consists of finer-grained plagioclase, clinopyroxene, volcanic glass, and opaque minerals displaying an overall porphyritic or vitrophyric texture. In some cases,

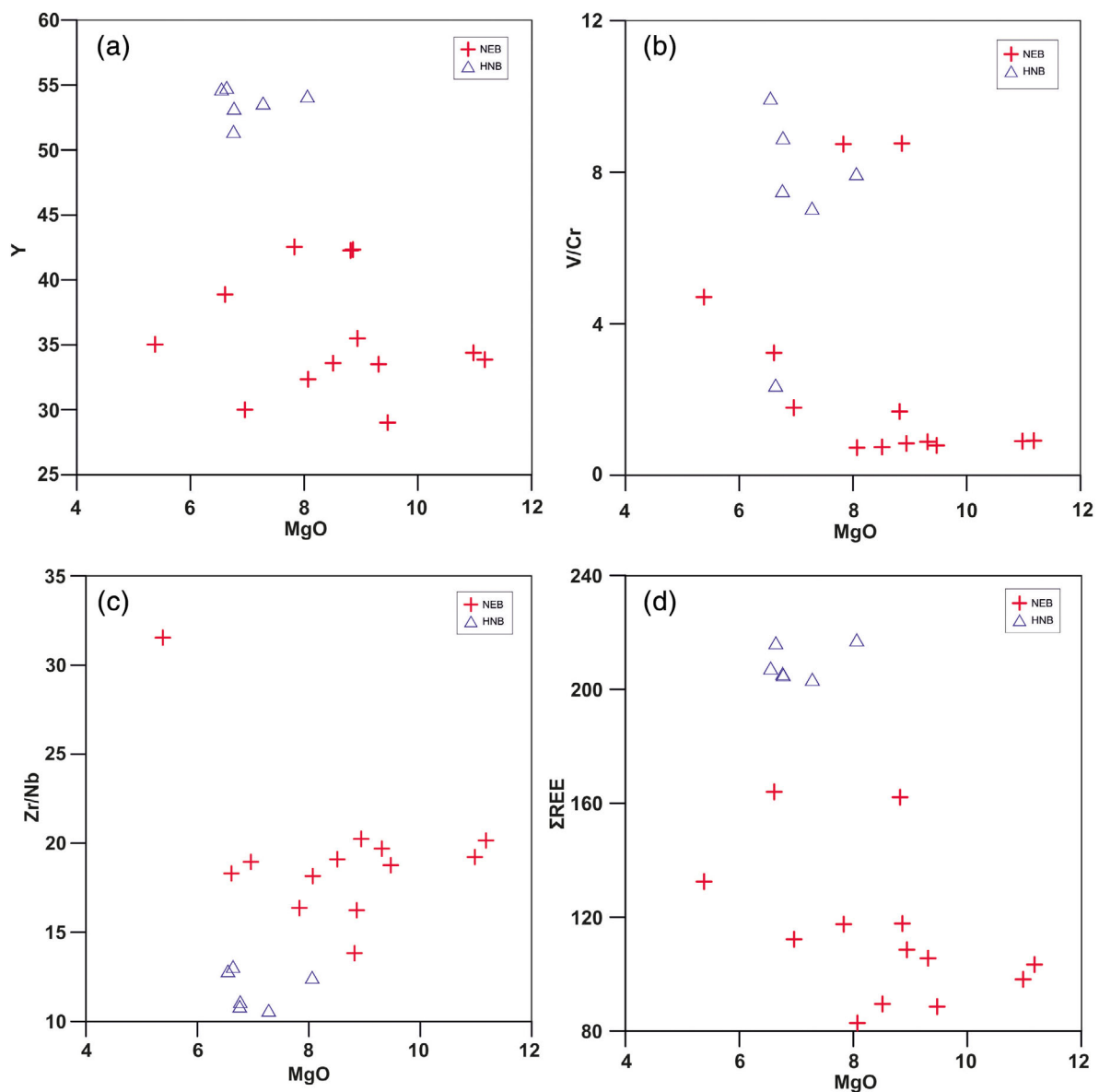


FIGURE 9 (a-d) Variations of different trace elements, their respective ratios, and total REE with respect to MgO for the analysed samples [Colour figure can be viewed at wileyonlinelibrary.com]

glomeroporphyritic texture has also been developed. In the ground-mass materials, ophitic or sub-ophitic and intergranular or intersertal textures are also noticed (Figure 3e). Vug and amygdaloidal structures are also common (Figure 3f).

5 | GEOCHEMISTRY

Major and trace element compositions of the mafic volcanic rocks of IOG (Figure 2) from Koira are given in Table 2. The IOG mafic volcanic rocks from the Koira region show SiO₂ content 46.03–55.31 wt %, while Al₂O₃ content is varying from 11.30–13.41 wt%. TiO₂ content spans from 1.12–2.50 wt%, whereas range of MgO is 5.38–11.18 wt%. The ranges of FeO^(t) and total alkalis (Na₂O + K₂O) vary from 11.07–15.17 wt% and 1.71–4.58 wt%, respectively. These are compositionally basalts to basaltic andesites (Figure 4a) in Total

alkali vs. silica diagram (after Le Bas et al., 1986). Moreover, they also display a transitional character between tholeiitic and calc-alkaline nature in the FeO^(t)-MgO-(Na₂O + K₂O) diagram (Figure 4b). In terms of (Zr + Y)-(TiO₂ × 100)-(Cr) triangular classification diagram (Davies et al., 1979), the plots of the mafic volcanic rocks occupy mostly a domain which is transitional between tholeiitic and calc-alkaline field (Figure 4c). The IOG basalts are characterized by both olivine normative and quartz normative compositions reflecting different degrees of saturation of precursor magmas. The Differentiation Index (D.I.) [normative quartz (Q) + orthoclase (Or) + albite (Ab) + nepheline (Ne) + kalsilite (Ks) + leucite (Lc)] (Thornton & Tuttle, 1960) for the studied samples range from 14.33 to 40.01 reflecting on higher degree of internal fractionation for the investigated samples. Solidification Index (S.I.) [100 × {MgO / (MgO + FeO + Fe₂O₃ + Na₂O + K₂O)}] (after Kuno, 1964) varying from 23.59 to

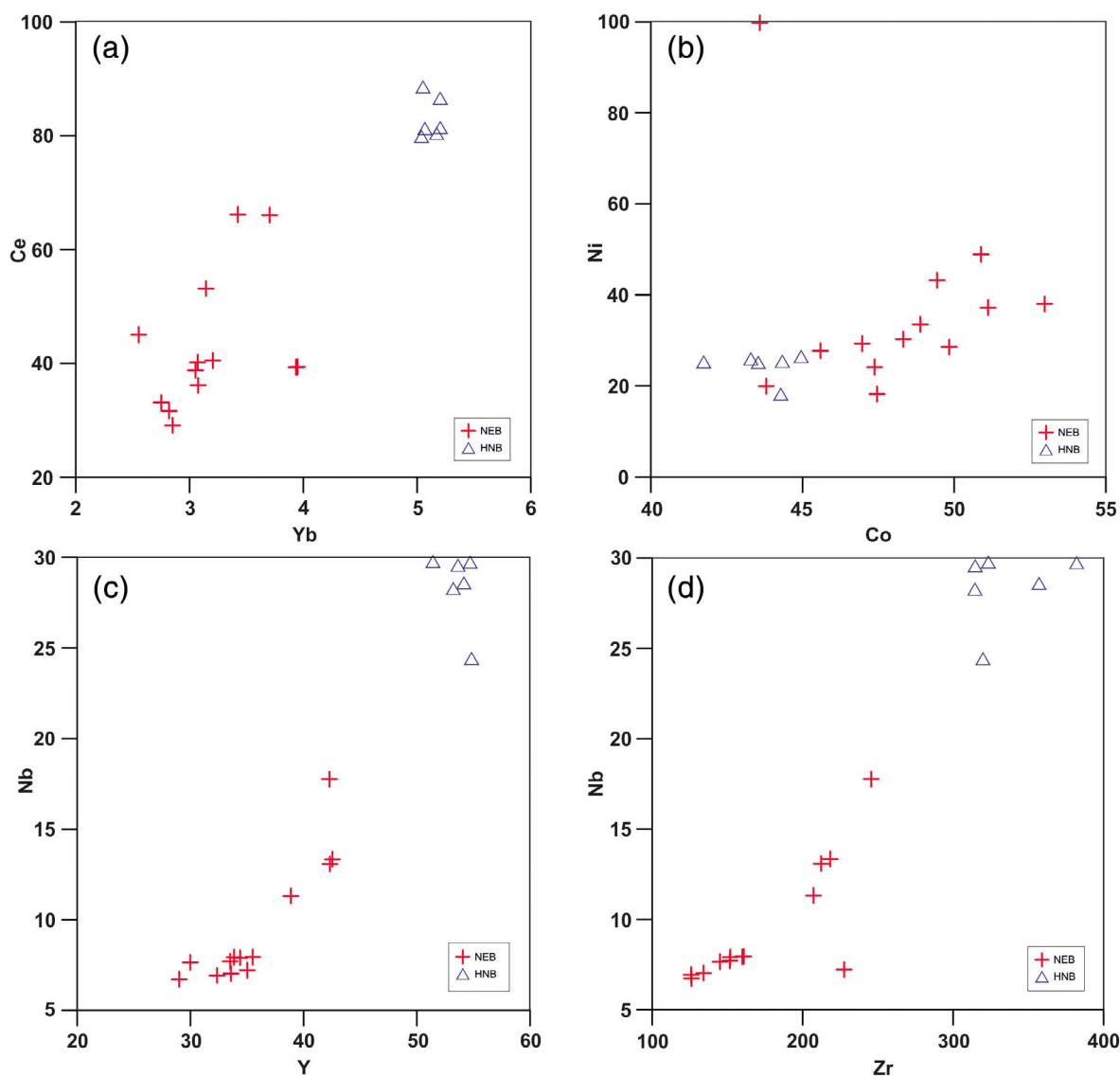


FIGURE 10 (a) Ce vs. Yb, (b) Ni vs. Co, (c) Nb vs. Y, and (d) Nb vs. Zr showing variations related to magmatic crystallization [Colour figure can be viewed at wileyonlinelibrary.com]

40.23 manifests prominent fractional crystallization during the evolution of individual lava flows.

Trace element chemistry for the studied IOG volcanic samples show distinct enrichment in Ba, Sr, Zr, Hf, Nb, Y, and Σ REE (Table 2). These IOG volcanic rocks show wide variation for Ba (76–608 ppm), Sr (86–968 ppm), Nb (6.7–29.8 ppm), Zr (126–382.1 ppm), and Σ REE (82.80–217.36 ppm), while Hf and Y show limit in range like 3.8–8.6 ppm and 29–54.8 ppm, respectively. In general, basalts erupted from mid-oceanic ridge will have \sim 3 ppm Nb; whereas OIBs will have \sim 48 ppm Nb; arc basalts generated at convergent margin will have \sim 8 ppm Nb, and plume basalts will have \sim 13 ppm Nb (Niu & O'Hara, 2003; Wilson, 1989). The Nb concentration in the studied samples range from 6.7–29.8 ppm. According to (Kerrich & Manikyamba, 2012), the Nb content ranging from 6.3–18 ppm are considered as NEB and above 20 ppm are classified as HNB. Based on Nb concentrations, the studied rocks are classified as Nb-enriched basalts (NEB; Nb > 7 ppm) and high-Nb basalts (HNB; Nb > 20 ppm). This classification-scheme has been used in subsequent geochemical

diagrams which are displaying overlapping geochemical signatures (for details see Section 6.1).

Certain trace element ratios namely Nb/U, Nb/La, and primitive mantle-normalized Nb/Th and Nb/La are useful to delineate the basalts of MORB, OIB, island arc tectonic settings (Castillo, 2009; Kerrich & Manikyamba, 2012). Investigated basalts plot within the fields of island arc basalts and Nb-enriched basalts (Figure 5a–c). Chondrite-normalized REE patterns for the studied NEB and HNB (Figure 6a) exhibit uniform LREE enrichment with relative MREE and HREE depletion and distinct Eu negative anomalies. Elevated $(La/Yb)_N$, $(La/Sm)_N$, $(Sm/Yb)_N$, and $(Gd/Yb)_N$ ratios commensurate with prominent LREE/HREE, LREE/MREE, and MREE/HREE fractionation, respectively. Primitive mantle-normalized incompatible trace element abundance patterns (Figure 6b) reflect enrichment in fluid/melt mobile LILE and LREE (e.g., Th, U, La, Ce, Nd) with relative depletion in fluid immobile HFSE manifested in terms of negative Nb-Ta anomalies. The NEB and HNB samples show lesser magnitude of negative Nb anomalies compared to normal arc basalts (Kerrich & Manikyamba, 2012).

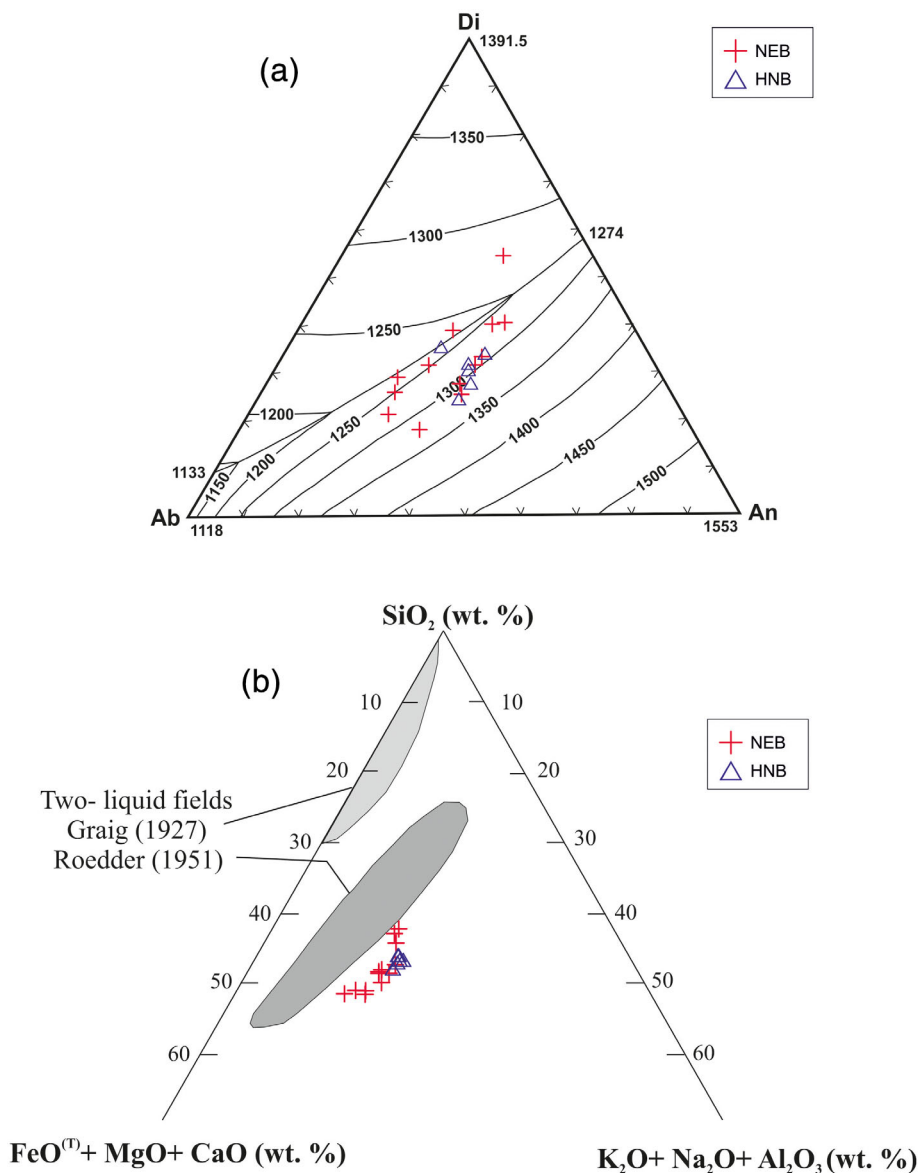


FIGURE 11 (a) The Diopside–Albite–Anorthite ternary diagram showing behaviour of plagioclase fractionation. (b) Plot of SiO_2 – $(FeO^{(T)} + MgO + CaO)$ – $(Na_2O + K_2O + Al_2O_3)$ for liquid immiscibility showing two-liquid fields suggested by Greig (1927) and Roedder (1951). The investigated samples plot near the two-liquid field suggested by Roedder (1951) [Colour figure can be viewed at wileyonlinelibrary.com]

$(La/Sm)_N$ values range between 1.94–3.30 for NEB, while it ranges from 3.62–3.77 for HNB. In case of $(Gd/Yb)_N$ ratio, it is found to be higher than 1 and varies between 1.05–1.46 for NEB and 1.10–1.38 for HNB. ΣREE is significantly higher and this ranges between 82.80–164 for NEB and 203.55–217.36 for HNB. REE patterns also point out that these Nb-enriched basalts were generated above the garnet stability field. Therefore, the rare-earth element patterns for the studied NEB and HNB (Figure 6a) can be attributed to inevitable influence of fractionation-differentiation from parent magma coupled with mantle-wedge metasomatism which is a common finding in Archean and post-Archean time (Wyman, Ayer, & Devaney, 2000). Further, our present study indicates that there is a role of partial melting for generation of parent melt which was also accompanied by fractional crystallization (Figure 7a,b). It has also been suggested in this paper (see Section 6.2) that parent-melt generation is associated with (wedge related) progressive ocean–continent convergence in this terrane. Polat & Kerrich (2001) demonstrated that such subduction-related Nb-enriched basalts characteristically display relatively higher LREE contents, slightly fractionated HREE behaviour [$(Gd/Yb)_N \sim 1.5$], and almost uniform Y content. Our observed values also put credence to this contention.

6 | DISCUSSION

6.1 | Petrogenesis: Roles of fractional crystallization and liquid immiscibility during magma differentiation

Geochemical variation diagrams are often used to understand the role of fractionation-differentiation from a parent magma (Cox, Bell, & Pankhurst, 1979). To decipher the nature of magmatic differentiation in the present study, several variation diagrams for major oxides, trace elements, and their respective ratios were attempted involving MgO as independent parameter for contrasting fractionation trends. CaO/Al_2O_3 vs. MgO diagram (Figure 8a) shows an initial rising trend with increasing MgO followed by a slightly declining trend at ~ 8 wt% MgO. The kink in the variation diagram (marked as “**”) has been produced by entry of a later phase mineral during magmatic crystallization. In the present scenario, the mineral responsible for producing such a kink is found to be clinopyroxene. The variation of SiO_2 vs. MgO shows a significant declining trend of SiO_2 with rising MgO and the controlling mineral is again found to be clinopyroxene (Figure 8b). The later entry of clinopyroxene in the crystallization regime (as reflected through a kink in the variation diagram) is supported by dominance of clinopyroxene in groundmass. It is, therefore, evident that geochemical characters and petrographic details support that these mafic volcanics are controlled by removal of plagioclase (from the parent magma) in the early stage of crystallization; this was followed by clinopyroxene and Fe-Ti oxides separation. TiO_2 vs. MgO diagram (after Condie, 2001) (Figure 7a) and Zr vs. Ni diagram (Figure 7b) for the investigated rocks shows combined effects of partial melting and fractional crystallization. In other words, melting of

the source mantle was followed by fractional crystallization. The trace element diagram involving Y vs. MgO (Figure 9a) follows similar

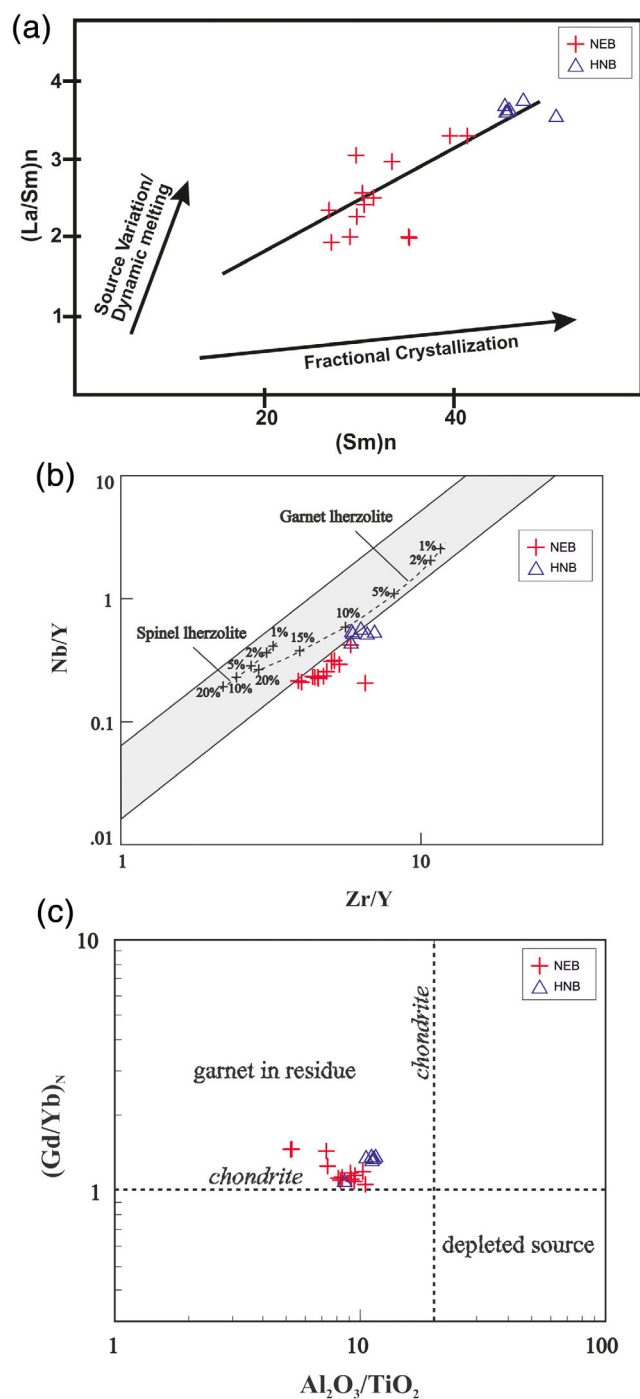


FIGURE 12 (a) Plots of $(La/Sm)_n$ vs. $(Sm)_n$ (after Jourdan et al., 2007) shows evidence of both melting and fractional crystallization. (b) Plots of Nb/Y vs. Zr/Y showing the mantle melting conditions. Fractional melting curves are shown for garnet and spinel lherzolite calculated according to the procedures of Fitton, Saunders, Norry, Hardarson, and Taylor (1997). Fields for basalts from Deccan Traps (data sources in Mahoney, 1988) are shown for reference. (c) Plots of $(Gd/Yb)_N$ vs. Al_2O_3/TiO_2 (after Arndt, 2003) for studied samples. The samples correspond to an enriched mantle source within the garnet stability field [Colour figure can be viewed at wileyonlinelibrary.com]

differentiation pattern for $\text{CaO}/\text{Al}_2\text{O}_3$ vs. MgO . The initial steady rise of Y with advent of differentiation (which is a common expectation in a magmatic regime) followed by distinct fall at ~ 8 wt% MgO has been documented. V/Cr vs. MgO (Figure 9b) shows increasing trend with continuous differentiation as expected in magmatic crystallization while Zr/Nb vs. MgO diagram (Figure 9c) gives negative pattern as a result of fractionation. Similarly, ΣREE vs. MgO diagram shows falling pattern of ΣREE with increasing MgO (Figure 9d). The ΣREE variation with respect to MgO suggests progressive enrichment of REE during the later stage of magmatic differentiation.

The variation of one of the LREEs (Ce) was plotted against representative HREE (Yb). The variations of Ce against Yb (Figure 10a) maintaining a sympathetic positive relation (due to equal ease of entry of both LREE and HREE in the crystal structure). However, the interrelation between Ni and Co for the investigated basaltic rocks (Figure 10b) shows a gentle increasing pattern indicating inadequate changes in the Ni/Co ratio during the course of magmatic crystallization. The behavioural pattern for Nb against Y and Zr , both show strong positive relation which are in support of fractionation history (Figure 10c,d).

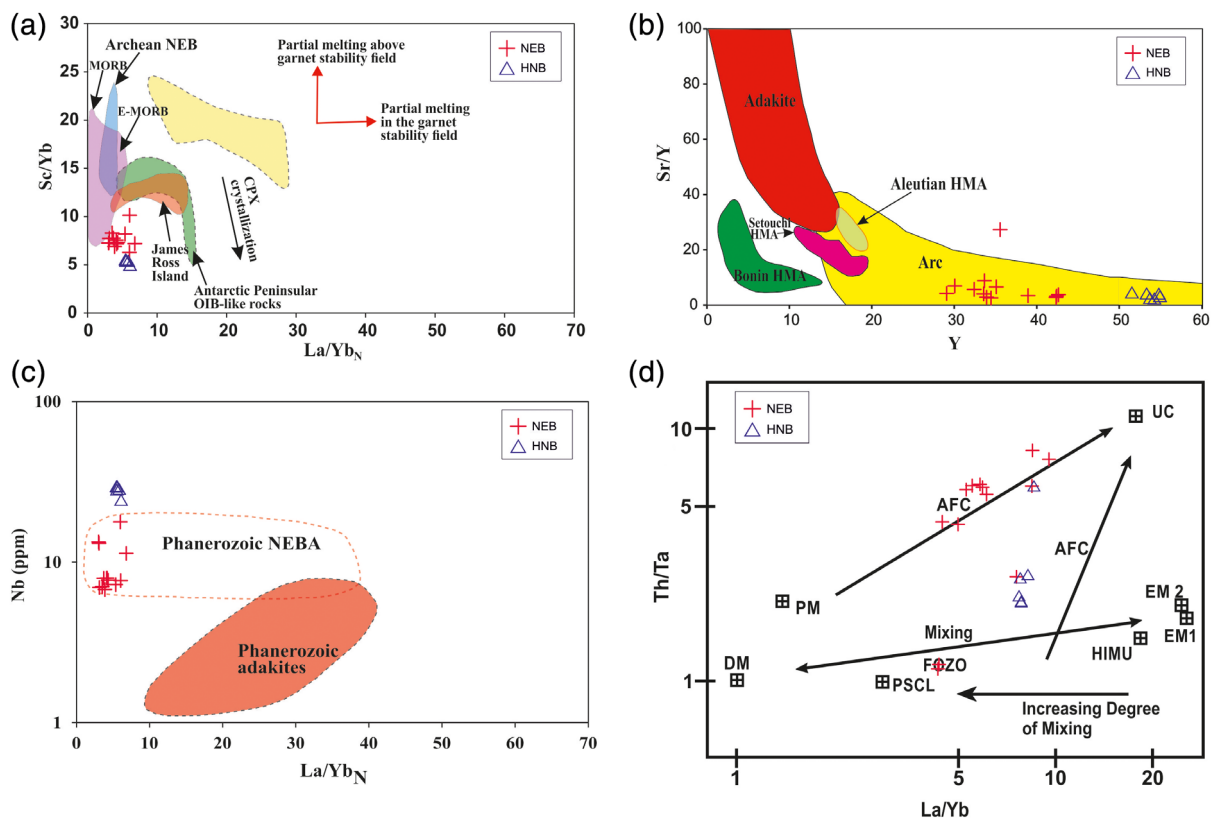


FIGURE 13 (a) Sc/Yb vs. $(\text{La}/\text{Yb})_N$ showing partial melting of the source mantle having residual garnet. (b) Sr/Y vs. Y discrimination figure with fields of arc, adakites, and high-Mg andesites from Aleutian, Setouchi, and Bonin islands in which the studied samples are falling in the field of Arc (after Tatsumi, 2006). (c) Nb vs. $(\text{La}/\text{Yb})_N$ of studied samples showing geochemical similarities with Phanerozoic equivalents (fields for Phanerozoic rocks are from Defant, Jackson, and Drummond (1992), McCarren and Smellie (1998), Sajona et al. (1996), and Stern and Kilian (1996)). (d) Th/Ta vs. La/Yb plot (after Condie, 2001) showing the plots of studied mafic volcanics and the distribution of mantle components. DM: depleted mantle, PM: primitive mantle, PSCL: post-Archean subcontinental lithosphere, FOZO: focal zone mantle, EM1 and EM2: enriched mantle sources, HIMU: high- μ source, UC: upper continental crust, AFC: assimilation-fractional crystallization trajectory. The basalts show enriched mantle parameter which has suffered upper continental crustal contamination [Colour figure can be viewed at wileyonlinelibrary.com]

In order to understand the nature of differentiation mechanism of the parent magma, textural studies give us important clues (Bose, 1997; Cox et al., 1979). In the present study, the textural pattern clearly indicates that the investigated mafic volcanics are distinctly plagioclase-phyric which suggests earlier separation (or fractional crystallization) of plagioclase. Such earlier fractionation of plagioclase has been corroborated by normative Diopside-Albite-Anorthite diagram (Morse, 1980) (Figure 11a) where almost all data of analysed mafic volcanics plot within plagioclase field which leads to culmination of the magma-composition to cotectic line. The degree of plagioclase separation is also deduced to be variable as documented from rock/chondrite pattern (Figure 6a) wherein most of the samples are showing distinct negative Eu anomalies while remaining are devoid of such anomalies.

Liquid immiscibility is one of the important differentiation mechanisms in many basaltic rocks, and evidence of such liquid immiscibility has been recorded in Deccan basalts (De, 1974; Ganguly et al., 2014). Greig (1927) and Roedder (1951) demarcated characteristic liquid immiscibility field (two liquid fields) in SiO_2 - (FeO^{t}) + MgO + CaO - $(\text{Na}_2\text{O} + \text{K}_2\text{O} + \text{Al}_2\text{O}_3)$ diagram (Figure 11b). The plots of investigated

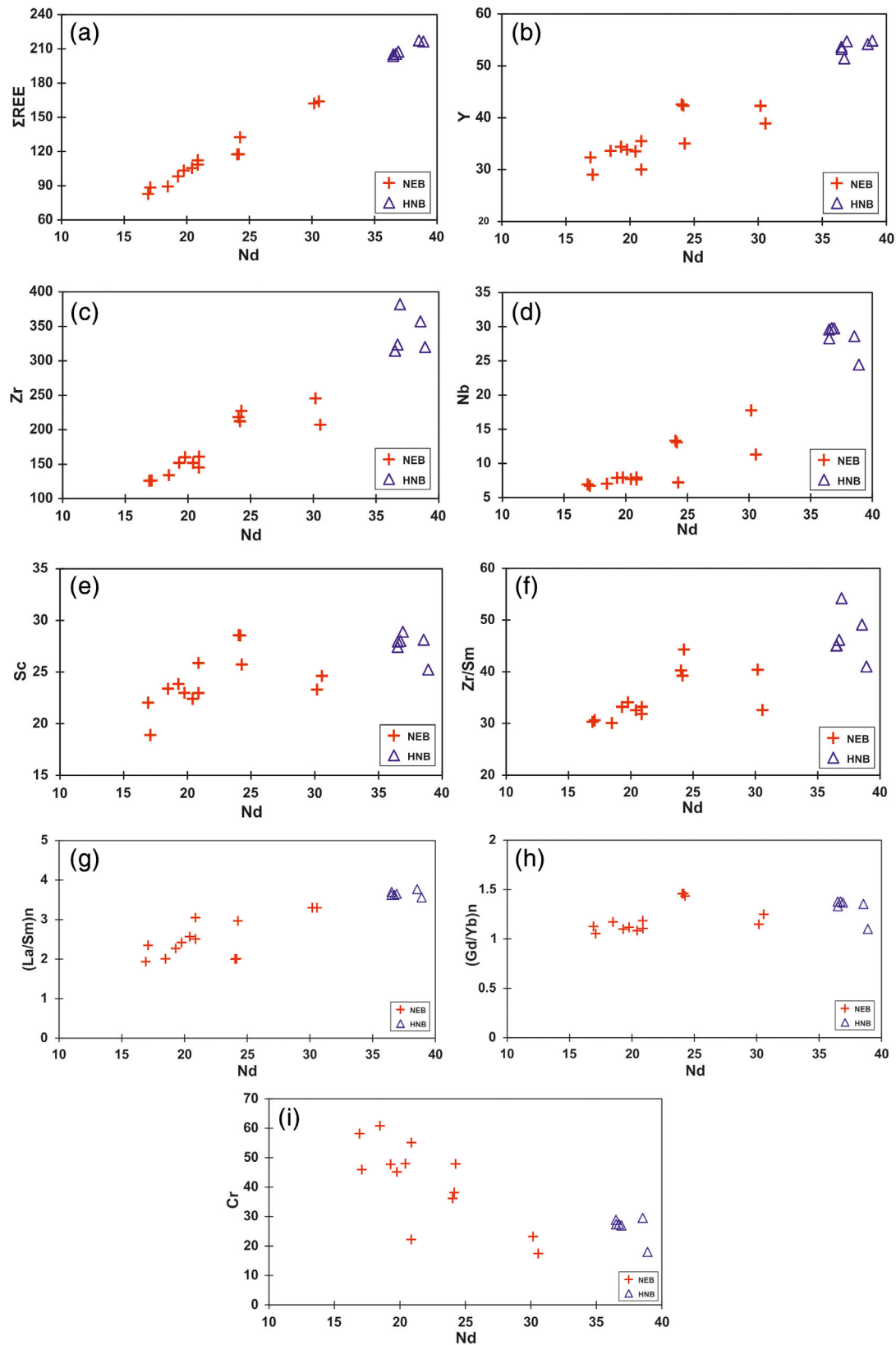


FIGURE 14 (a–i) Variations of different trace elements, their respective ratios (including primitive normalized) and total REE with respect to Nd for the analysed samples [Colour figure can be viewed at wileyonlinelibrary.com]

IOG mafic volcanics in this triangular diagram, lie very close to liquid immiscibility field of Roedder (1951) suggesting that silicate liquid immiscibility played an important role during differentiation; in fact, this has given rise to high FeO^t (>12.6 wt%) and low FeO^t (<12.6 wt %) sub types (see Table 2).

6.2 | Subduction processes and magma generation

Trace and REE chemistry of these rocks exemplified by LILE-LREE enriched HFSE depleted characteristics (Figure 6a,b) attribute their genesis from a source mantle enriched by subduction processes. The fractionated LREE/HREE and MREE/HREE patterns adduce a garnet-bearing mantle source and melt extraction with garnet in the residue. Chondrite-normalized negative Eu anomalies in conjunction with primitive mantle-normalized negative anomalies for Sr suggest plagioclase fractionation in the mantle restite or origin of precursor magmas from a plagioclase-free mantle source (Kaimura & Sano, 2012; Prat, Ganne, & Lombard, 2003). Negative Nb-Ta anomalies with respect to primitive mantle compositions discard the possibility of OIB-type plume origin. LILE-LREE enrichment with HFSE depletion, negative Nb-Ta anomalies, and positive Zr-Hf anomalies suggest involvement of continental lithospheric mantle (CLM) and crustal contamination (James, 1981; Lassiter & Luhr, 2001). The positive Zr-Hf anomalies noticed for both NEB and HNB samples (Figure 6b) are controlled by their mantle source characteristics, especially involving presence of rutile and amphibole. Experimental studies by Ionov & Hofmann (1995) and Morisset, Scoates, & Weis (2006) on rutile and amphibole indicate that Zr and Hf are compatible (in varying degree) in both these two minerals. During plate convergence setting (in water-ambient condition), presence of these two minerals plays vital role in producing positive Zr and Hf anomaly pattern. Low Th contents and Th/Ce ratios support the contention of subducted slab melting rather than magma generation by lower crustal melting. The lower Ce/Pb and higher Ba/La ratios for studied NEB and HNB as compared to OIB and MORB substantiate subduction processes and input from subduction components in the source mantle. It has been suggested that melt generation is related to slab-derived fluids and/or slab-derived melts and mantle metasomatism (Andrew, Hensen, Dunlop, & Agnew, 1995; Cai et al., 2014; Hastie, Mitchell, Kerr, Minifie, & Millar, 2011; Médard, Schmidt, Schiano, & Ottolini, 2006).

TABLE 3 Selected incompatible trace element ratios of mafic volcanics of IOG and their petrogenetic significance

Ratio	Min	Max	Comments on source parameter (Weaver, 1991)
Zr/Nb	10.64	31.54	Continental crust, EM1 OIB
La/Nb	1.26	3.27	Continental crust, EM1 OIB
Ba/Nb	6.13	73.10	Continental crust, HIMU, EM1 OIB, EM2 OIB
Ba/Th	24.36	293.20	Continental crust, HIMU, EM1 OIB, EM2 OIB
Rb/Nb	0.50	6.29	Continental crust, EM1 OIB, EM2 OIB
K/Nb	196.70	1,438.23	Continental crust, EM1 OIB, EM2 OIB
Th/Nb	0.12	0.51	Continental crust, EM1 OIB, EM2 OIB
Th/La	0.09	0.19	Continental crust, HIMU, EM1 OIB, EM2 OIB
Ba/La	4.30	30.31	Continental crust, HIMU, EM1 OIB, EM2 OIB

Chondrite-normalized REE patterns exhibit uniform enrichment in LREE. In order to deduce the conditions for parent melt generation, (La/Sm)_n vs. (Sm)_n plot (after Jourdan et al., 2007) was used (Figure 12a) which clearly shows role of both melting and fractional crystallization were involved in order to produce the mafic volcanic rocks. Trace element composition has been used to constrain extent of mantle melting (Lassiter, DePaolo, & Mahoney, 1995; Reichow, Saunders, White, Al'Mukhamedov, & Medvedev, 2005). The investigated samples (for both NEB and HNB) are plotted in Nb/Y vs. Zr/Y diagram (Figure 12b) adopting the melting calculation of Fitton et al. (1997) wherein the samples lie close to the melting curve of garnet peridotite suggesting their genesis by ~10%–20% melting in the garnet lherzolite melting domain. (Gd/Yb)_n values of the investigated mafic volcanics show a span from 1.05 to 1.46 and this is consistent with MREE/HREE fractionation. The (Gd/Yb)_n ratios of investigated samples have been plotted against their respective $\text{Al}_2\text{O}_3/\text{TiO}_2$ value (Figure 12c) (Arndt, 2003) in order to determine the source composition and melting domain for genesis of parent magma. This clearly indicate presence of garnet in the residue. Sc/Yb vs. (La/Yb)_N variations (Figure 13a) also suggest that residual garnet was present in the source mantle for the studied NEB and HNB samples. The studied samples with uniformly low Sr/Y plot fall in the arc field in Figure 13b.

Several processes namely melt extraction events, refertilization by crustal recycling, and subduction related fluid influx induced metamorphism play pertinent role during chemical evolution of mantle (Jean, Shervais, Choi, & Mukasa, 2010). Mantle re-enrichment mechanisms are primarily associated with lithospheric plate movements and oceanic plate subduction is an integral process triggering recycling and geochemical exchange through ocean-crust-mantle interactions (Brandon, Walker, Morgan, Norman, & Prichard, 1998; Liu et al., 2010; Wilde, Zhou, Nemchin, & Sun, 2003). Subduction zone magmatism in geological space and time records a remarkable geochemical diversity equitable with types and stages of subduction, extent of slab-mantle interactions, input from subductions components. Geochemical signatures suggest that the genesis of NEB and HNB is attributable to slab-melting and wedge hybridization processes during matured stages of subduction (Gray & Pysklywec, 2012). The Nb vs. (La/Yb)_N and Th/Ta vs. La/Yb variations for the studied NEB and HNB from Koira have been shown in Figure 13c,d. It is evident that the mafic volcanic rocks from Koira are well within the range of Phanerozoic Nb-enriched basaltic andesites (Figure 13c). Several workers (Mibe, Kawamoto,

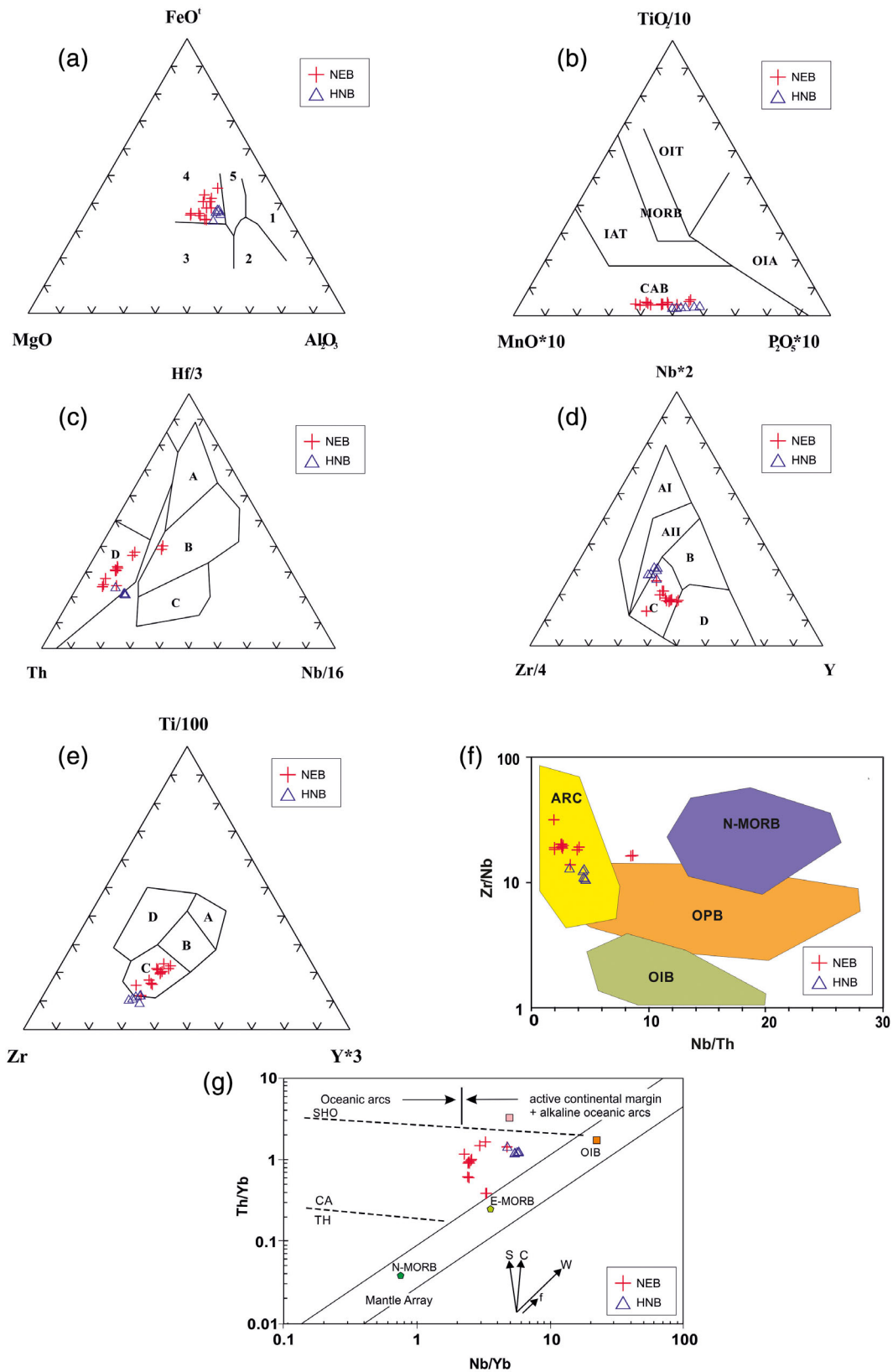


FIGURE 15 Legend on next page.

Matsukage, Fei, & Ono, 2011; Thomson, Walter, Kohn, & Brooker, 2016; Walowski, Wallace, Hauri, Wada, & Clyne, 2015) were of the opinion that genesis of such rocks have calc-alkaline magmatic parentage caused due to partial melting of garnet peridotite mantle wedge hybridized by slab-derived melts. Further, this phenomenon is especially found during matured stages of subduction (Gray & Pysklywec, 2012). Slab melts migrating through a mantle wedge fractionate, hybridize, and metasomatize the peridotite whereby the original minerals of the peridotite (olivine, orthopyroxene, clinopyroxene, and spinel) are broken down and replaced by precipitating Nb and Ti-enriched pargasitic amphibole, garnet, phlogopite, Na-rich clinopyroxene, and Fe-enriched orthopyroxene and Na-plagioclase at low pressures (Hastie et al., 2011; Kepezhinskas, Defant, & Drummond, 1995; Prouteau, Scaillet, Pichavant, & Maury, 2001; Rapp, Shimizu, Norman, & Applegate, 1999). In slightly altered mafic rocks, the element Nd is used as a measure of assessing the degree of fractional crystallization of parent magma (or degree of partial melting of source). In this approach, to understand the mantle wedge fractionation Nd used as an index of fractional crystallization and against Nd, several alteration-resistant elements are plotted in bivariate diagrams. This method was successfully used by Kerrich & Manikyamba (2012) to constrain genesis of subduction-related Nb-enriched basalts of Dharwar Craton of Southern India. In this view, an attempt has been made here to evaluate the nature of variation of several alteration-resistant elements (and element-ratios) against Nd to decipher fractionation history or melting condition (Figure 14). From Figure 14a–h, it is apparent that $\sum\text{REE}$, Y, Zr, Nb, Sc, Zr/Sm, (La/Sm)_n, and (Gd/Yb)_n show progressively rising trends (with increase in Nb) from NEB to HNB. In other words, all the above-stated elements (or element ratios) were becoming progressively enriched in HNB which suggests geochemically more advanced nature of melts in HNB, related to separate (greater) degree of melting. The declining trend of Cr with increasing Nd (Figure 14i) also suggests separate pulses of melting corresponding to NEB and HNB. Two contrasting situations are possible based on melt: rock ratio (Hastie et al., 2011; Rapp et al., 1999; Sajona et al., 1993; Sajona et al., 1996). If this ratio is high enough, the resultant hybridized melt will have lower SiO₂ and higher MgO, Ni, and Cr contents and eventually produce adakite. On the other hand, if the ratio is lower, the slab melts are consumed and the metasomatized peridotite can suffer subsequent partial melt to generate adakite/high-Mg andesite magmas. The model of Sajona et al. (1993, 1996), which is

also similar to one proposed by Kepezhinskas et al. (1995) and Kepezhinskas et al. (1996), proposes that the first slab-derived melts are produced at a depth of 75–85 km. On ascent, they react with the mantle wedge to produce the aforementioned mineral assemblage in a metasomatized spinel peridotite. The metasomatic minerals will subsequently scavenge several trace elements; for example, amphibole would persistently take Ti, Nb, and Ta from continually ascending slab-melts. This process would continue until the (ascending) slab melt is subsequently convected to a sufficient depth. At such great depth, amphibole (and accessory rutile) breaks down and facilitates partial melting of the wedge and generation of HNBs and NEBs. A similar model is proposed for the generation of the studied NEB and HNB of IOG volcanics from Koira. The compositional spectrum recorded by the IOG volcanic rocks of Nb-enriched and high-Nb chemistry suggests variable slab-mantle interactions and mantle wedge metasomatism by dehydration and melting of subducted oceanic slab concomitant with progressive maturation of ocean-continent subduction process. Weaver (1991) used several selected incompatible trace element ratios to constrain the mantle source characters. This method is found to be effective and reveals precise result similar to that obtained while using radiogenic isotope ratio data. In this view, these incompatible trace element ratios were used elsewhere for bracketing mantle sources (Chaudhuri et al., 2014; Ray et al., 2013). Certain incompatible trace element ratios for the studied mafic volcanic rocks (Table 3) invoke an enriched (EM1-EM2 type) mantle component in source and almost all trace element ratios unequivocally suggest effects of continental crustal assimilation of parent magma. Plot of Th/Ta vs. La/Yb (after Condie, 2001) for the investigated samples in Figure 13d reflects crustal contamination of primitive mantle through the process of AFC. The geochemical characteristics of the IOG volcanic rocks from Koira attest to crustal assimilation through intracrustal melting of continental arc crust by ascending calc-alkaline NEB and HNB melts.

6.3 | Tectonic implications

The IOG volcanics have earlier been designated as “ocean floor basalts” or “moderate Mg-type tholeiites” (Saha, 1994); however, an intra-oceanic arc setting with signature of crustal contamination has been advocated for these rocks in recent times (Singh et al., 2016). On the basis of FeO^(t)-MgO-Al₂O₃ diagram (Figure 4b), the studied

FIGURE 15 (a) MgO-FeO^(t)-Al₂O₃ discrimination diagram for studied samples occupying ocean island field (after Pearce et al., 1977). 1 = spreading centre island, 2 = orogenic, 3 = ocean ridge and floor, 4 = ocean island, 5 = continental. (b) MnO*10⁻²-P₂O₅*10⁻²-TiO₂/10 triangular diagram (after Mullen, 1983) classifying the mafic volcanic rocks as calc-alkaline basalt (CAB). MORB = mid-ocean-ridge-basalt, CAB = calc-alkaline basalt, OIT = ocean island tholeiites, OIA = ocean island alkaline basalt, IAT = island arc tholeiites. (c) The mafic volcanic samples displaying a calc-alkaline basalt affinity in terms of Th- Hf/3- Nb/16 compositional variations (after Wood, 1980). A = N-MORB, B = E-MORB, C = within-plate alkali basalt, D = volcanic arc basalt (calc-alkaline). (d) Tectonic discrimination Zr/4- Nb*2- Y diagram (after Meschede, 1986) for studied mafic volcanics. Data plots characteristically occupy volcanic arc basalt field. AI = within-plate alkali basalt, AII = within-plate alkali basalt and within-plate tholeiites, B = P-MORB, D = N-MORB, C = within-plate tholeiites and volcanic arc basalt. (e) Zr-Ti/100-Y*3 discrimination diagram for studied samples (after Pearce & Cann, 1973). The investigated data plots are found to be occupied mostly in the calc-alkaline field. A = island arc tholeiites, B = MORB, C = calc-alkali basalt, D = within-plate basalt. (f) Zr/Nb vs. Nb/Th diagram (after Condie, 2005) displaying arc characteristics for mafic volcanic samples. (g) Plots of investigated samples of NEB and HNB in the Th/Yb vs. Nb/Yb diagram (after Pearce, 2008) depicting calc-alkaline arc affinity [Colour figure can be viewed at wileyonlinelibrary.com]

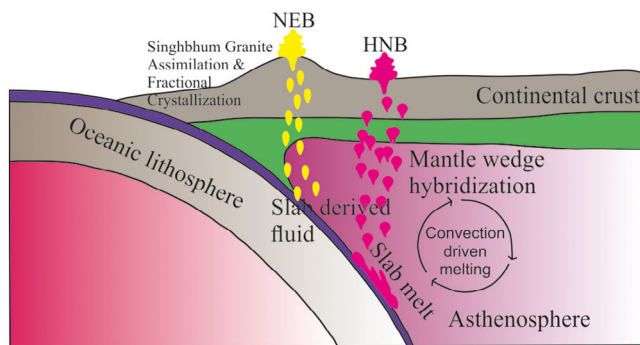


FIGURE 16 Schematic tectonic model explaining eruption of Nb-enriched basalts and high-Nb basalts (relevant to present study) in a subduction zone setting by wedge melting and sub-arc mantle under the influence of slab derived melts [Colour figure can be viewed at wileyonlinelibrary.com]

rocks reveal an affinity which is transitional between tholeiitic and calc-alkaline character; however, their petrogenetic control could be better understood using tectonic discrimination diagrams. On $\text{MgO-FeO}^{(t)}\text{-Al}_2\text{O}_3$ diagram (Pearce, Gorman, & Birkett, 1977), the data plots distinctly cluster in the oceanic island arc field (Figure 15a). The $\text{MnO}^*10\text{-P}_2\text{O}_5^*10\text{-TiO}_2/10$ plot (Mullen, 1983) (Figure 15b) corroborates a continental arc basalt (CAB) affinity for the studied IOG volcanic rocks. High-field-strength elements (HFSE) and their ratios serve as effective geochemical proxies to constrain tectonic environments of mantle derived rocks. $\text{Th-Hf}/3\text{-Nb}/16$ (Wood, 1980) and $\text{Zr}/4\text{-Nb}^2\text{-Y}$ (Meschede, 1986) compositions endorse distinct volcanic arc-related calc-alkaline attributes for these rocks (Figure 15c,d). The IOG volcanic rocks of Koira occupy the calc-alkaline basalt field on $\text{Zr-Ti}/100\text{-Y}^3$ triangular plot (Figure 15e; Pearce & Cann, 1973) and correspond to the arc field of Zr/Nb vs. Nb/Th diagram (Figure 15f; Condie, 2005). In concurrence with these observations, Th/Yb vs. Nb/Yb plot (Figure 15g; Pearce, 2008), it is suggested that subduction components made a pronounced contribution for the genesis of parent magmas at an active continental margin setting.

7 | CONCLUSIONS

1. The investigated IOG mafic volcanic rocks from Koira sector, Singhbhum Craton are mostly plagioclase-phyric while clinopyroxene (and minor plagioclase, volcanic glass, and ilmenite) constitutes the groundmass.
2. Geochemical attributes classify these volcanics as NEB and HNB with pronounced signatures of contribution from subduction-derived fluids and melts.
3. Parental magma for NEB and HNB was derived by partial melting (of approximately 10%–20%) of an enriched garnet lherzolite (with minor presence of amphibole and rutile) wedge mantle source that was metasomatized and hybridized by slab-derived fluids and melts.
4. The rocks show evidence of AFC of precursor melts thereby invoking melting of continental arc crust.
5. Both partial melting and fractional crystallization were responsible for petrogenesis of the IOG mafic volcanics.
6. The fractional crystallization was documented by separation of early formed plagioclase (varied degree of separation) which was followed by separation of clinopyroxene and minor plagioclase.
7. Liquid immiscibility has played a role in differentiation mechanism for the IOG mafic volcanics and this immiscibility has led to presence of high FeO and low FeO subtypes within IOG mafic volcanics.
8. These rocks have a transitional character between tholeiitic and calc-alkaline basaltic parentage with an affinity to an active continental margin setting.
9. The NEB and HNB from IOG volcanics of Koira Sector preserve distinct geochemical signatures of matured stage of subduction, slab melting, and magma generation at an Archean ocean–continent convergent margin setting (Figure 16).

ACKNOWLEDGEMENTS

This work is an outcome of collaborative research project from Department of Science and Technology (SR/S4/ES-510/2010) for Department of Geology, University of Calcutta and National Geophysical Research Institute (NGRI), Hyderabad and forms a part of the Ph.D. thesis work of MP. The authors are thankful to authorities of University of Calcutta and NGRI for according necessary permission. CM thank Dr. V. M. Tiwari, Director, CSIR-NGRI for permission to publish this work and funding from GeoMet (MLP 0002 FBR2-EVSSKB). Drs. Keshav Krishna and Satyanarayanan are thanked for providing the analytical data. The authors are grateful to anonymous journal-reviewers (for providing incisive but helpful comments) and Prof. N.V. Chalapathi Rao for his erudite editorial- handling.

CONFLICT OF INTEREST

There is no conflict of interest between the authors. All the authors have read both the initial and final version of the manuscript before submission. They all have agreed to submit this paper to Geological Journal.

PEER REVIEW

The peer review history for this article is available at <https://publons.com/publon/10.1002/gj.3944>

ORCID

Jyotiskanar Ray  <https://orcid.org/0000-0002-2004-9907>

C. Manikyamba  <https://orcid.org/0000-0003-4736-4306>

REFERENCES

- Acharyya, S. K. (1993). Greenstones from Singhbhum Craton, their Archean character, oceanic crustal affinity and tectonics. *Proceedings of the National Academy of Sciences, India, Section A: Physical Sciences*, 63A, 211–222.
- Acharyya, S. K., Gupta, A., & Orihashi, Y. (2010). New U–Pb zircon ages from Palaeo-Mesoarchean TTG gneisses of the Singhbhum Craton, eastern India. *Geochemical Journal*, 44, 81–88.

- Andrew, A. S., Hensen, B. J., Dunlop, A. C., & Agnew, P. D. (1995). Oxygen and hydrogen isotope evidence for the origin of platinum-group element mineralization in Alaska-type intrusions at Fifield, Australia. *Economic Geology*, 90, 1831–1840.
- Arndt, N. (2003). Komatiites, kimberlites, and boninites. *Journal of Geophysical Research*, 108, 1–11.
- Barnes, S. J., & Van Kranendonk, M. J. (2014). Archean andesites in the east Yilgarn Craton, Australia: Products of plume-crust interaction? *Lithosphere*, 6, 80–92.
- Basu, A. R., Bandyopadhyay, P. K., Chakraborti, R., & Zou, H. (2008). Large 3.4 Ga Algoma type BIF in the Eastern Indian Craton. Goldschmidt Conference Abstract Volume. *Geochimica et Cosmochimica Acta*, 72, A59.
- Bédard, J. H. (2018). Stagnant lids and mantle overturns: Implications for Archean tectonics, magmagenesis, crustal growth, mantle evolution, and the start of plate tectonics. *Geoscience Frontiers*, 9, 19–49.
- Bleeker, W., & Ernst, R. E. (2006). Short lived mantle generated magmatic events and their dyke swarms: The key unlocking Earth's palaeogeographic record back to 2.6 Ga. In E. Hanski, S. Mertanen, T. Ramo, & J. Vuollo (Eds.), *Dyke Swarms- time markers of crustal evolution* (pp. 3–26). Rotterdam, the Netherlands: August Aimé Balkema Publishers.
- Bose, M. K. (1997). *Igneous Petrology*, Calcutta, India: The World Press Private Limited 568p.
- Bose, M. K. (2000). Mafic-ultramafic magmatism in the eastern Indian craton - A review. *Geological Survey of India, Special Publication*, 55, 227–258.
- Bose, M. K. (2009). Precambrian mafic magmatism in the Singhbhum Craton, Eastern India. *Journal of Geological Society of India*, 73, 13–35.
- Brandon, A. D., Walker, R. J., Morgan, J. W., Norman, M. D., & Prichard, H. M. (1998). Coupled ^{186}Os and ^{187}Os evidence for core-mantle interaction. *Science*, 280, 1570–1573.
- Cai, K., Sun, M., Xiao, W., Yuan, C., Zhao, G., Long, X., ... Zhou, K. (2014). Petrogenesis of Late Palaeozoic tholeiitic, Nb-enriched, calc-alkaline and adakitic rocks in Southwestern Mongolia: Implications for intra-oceanic arc evolution. *Lithos*, 202–203, 413–428.
- Castillo, P. R. (2009). Origin of Nb-enriched basalts and adakites in Baja California, Mexico, revisited: Reply. *Geological Society of America Bulletin*, 121(9–10), 1470–1472.
- Chaudhuri, S., Ray, J., Koeberl, C., Thöni, M., Dutta, R., Saha, A., & Banerjee, M. (2014). Petrology and geochemistry of the ultramafic-mafic Mawput complex, Meghalaya: A Sylhet trap differentiation centre in northeastern India. *Geological Journal*, 49, 111–128.
- Chaudhuri, T. (2020). A review of Hadean to Neoproterozoic crust generation in the Singhbhum Craton, India and possible connection with Pilbara Craton, Australia: the geochronological perspective. *Earth-Science Reviews*, 202, 103085. <https://doi.org/10.1016/j.earscirev.2020.103085>
- Chaudhuri, T., Mazumder, R., & Arima, M. (2015). Petrography and geochemistry of Mesoarchean komatiites from the eastern Iron Ore belt, Singhbhum Craton, India, and its similarity with 'Barberton type komatiite'. *Journal of African Earth Sciences*, 101, 135–147.
- Chaudhuri, T., Wan, Y., Mazumder, R., Ma, M., & Dunyi Liu, D. (2018). Evidence of enriched, hadean mantle reservoir from 4.2–4.0 Ga zircon xenocrysts from palaeoarchean TTGs of the Singhbhum Craton, eastern India. *Scientific Reports*, 8, 7069. <https://doi.org/10.1038/s41598-018-25494-6>
- Coffin, M. F., & Eldholm, O. (1994). Large igneous provinces: Crustal structure, dimensions and external consequences. *Reviews of Geophysics*, 32, 1–36.
- Condie, K. C. (1990). Geochemical characteristics of Precambrian basaltic greenstones. In R. P. Hall & D. J. Hughes (Eds.), *Early Precambrian basic magmatism* (pp. 11–39). New York, NY: Capmann and Hall.
- Condie, K. C. (1999). Mafic crustal xenoliths and the origin of the lower continental crust. *Lithos*, 46, 95–101.
- Condie, K. C. (2001). *Mantle plumes and their record in earth history*. London, UK: Cambridge University Press 305p.
- Condie, K. C. (2005). High field strength element ratios in Archean basalts: A window to evolving sources of mantle melting? *Lithos*, 79, 491–504.
- Cox, K. G., Bell, J. D., & Pankhurst, R. J. (1979). *The interpretation of igneous rocks*. London, UK: George Allen & Unwin Publishers Ltd 450p.
- Davies, J. F., Grant, R. W. E., & Whitehead, R. E. S. (1979). Immobile trace elements and Archean volcanic stratigraphy in the Timmins mining area, Ontario. *Canadian Journal of Earth Sciences*, 16, 305–311.
- De, A. (1974). Silicate liquid immiscibility in the Deccan traps and its petrogenetic significance. *Geological Society of America Bulletin*, 85(3), 471–474.
- De Wit, M. J., & Ashwal, L. D. (1995). Greenstone belts, what are they? *South African Journal of Geology*, 98, 505–520.
- Defant, M. J., Jackson, T. E., & Drummond, M. S. (1992). The geochemistry of young volcanism throughout western Panama and southeastern Costa Rica: An overview. *Journal of the Geological Society, London*, 149, 569–579.
- Dey, S., Topno, A., Liu, Y., & Zong, K. (2017). Generation and evolution of Palaeoarchean continental crust in the central part of the Singhbhum Craton, eastern India. *Precambrian Research*, 298, 268–291.
- Dostal, J., & Mueller, W. U. (2013). Deciphering an Archean mantle plume: Abitibi greenstone belt, Canada. *Gondwana Research*, 23, 493–505.
- Eriksson, P. G., Mazumder, R., Catuneanu, O., Bumby, A. J., & Ountsche Ilondo, B. (2006). Precambrian continental freeboard and geological evolution: A time perspective. *Earth-Science Reviews*, 79, 165–204.
- Fitton, J. G., Saunders, A. D., Norry, M. J., Hardarson, B. S., & Taylor, R. N. (1997). Thermal and chemical structure of the Iceland plume. *Earth and Planetary Science Letters*, 153, 197–208.
- Ganguly, S., Ray, J., Koeberl, C., Saha, A., Thöni, M., & Balaram, V. (2014). Geochemistry and petrogenesis of lava flows around Linga, Chhindwara area in the Eastern Deccan Volcanic Province (EDVP), India. *Journal of Asian Earth Sciences*, 91, 174–193.
- Ganguly, S., Santosh, M., & Manikyamba, C. (2019). An appraisal of geochemical signatures of komatiites from the greenstone belts of Dharwar Craton, India: Implications for temporal transition and Archean upper mantle hydration. *Geological Journal*, 54(5), 3088–3111. <https://doi.org/10.1002/gj.3532>
- Ganguly, S., & Yang, Q. Y. (2018). Greenstone belts and their mineral endowment: Preface. *Geoscience Frontiers*, 9, 599–601.
- Ghose, N. C., & Saha, A. (2018). Vestiges of older greenstone in Mesoarchean Chakradharpur granite gneiss, Singhbhum Craton, India: Implications for plume-lithosphere interaction at rifted cratonic margin. *Geological Journal*, 54, 1–23. <https://doi.org/10.1002/gj.3271>
- Ghosh, R., Vermeesch, P., Gain, D., & Mondal, R. (2019). Genetic relationship among komatiites and associated basalts in the Badampahar greenstone belt (3.25–3.10Ga), Singhbhum Craton, Eastern India. *Precambrian Research*, 327, 196–211.
- Gray, R., & Pysklywec, R. N. (2012). Geodynamic models of mature continental collision: Evolution of an orogen from lithospheric subduction to continental retreat/delamination. *Journal of Geophysical Research*, 117, B03408. <https://doi.org/10.1029/2011jb008692>
- Greig, J. W. (1927). Immiscibility in silicate melts. *American Journal of Science*, 13(1–44), 133–154.
- Harlan, S. S., Heaman, L. M., LeCheminant, A. N., & Premo, W. R. (2003). Gunbarrel mafic magmatic event: A key 780 Ma time marker for Rodinia plate reconstruction. *Geology*, 31, 1053–1056.
- Hastie, A. R., Mitchell, S. F., Kerr, A. C., Minifie, M. J., & Millar, I. L. (2011). Geochemistry of rare high-Nb basalt lavas: Are they derived from a mantle wedge metasomatized by slab melts? *Geochimica et Cosmochimica Acta*, 75, 5049–5072.
- Heaman, L. M. (2008). Precambrian Large Igneous Provinces: An overview of geochronology, origin and impact on earth evolution. *Journal of Geological Society of India*, 72, 15–34.
- Heaman, L. M., & LeCheminant, A. N. (1993). Paragenesis and U-Pb systematics of baddeleyite (ZrO₂). *Chemical Geology*, 110, 95–126.
- Ionov, D. A., & Hofmann, A. W. (1995). Nb-Ta rich mantle amphiboles and micas: Implications for subduction-related metasomatic trace element fractionations. *Earth and Planetary Science Letters*, 131, 341–356.
- Irvine, T. N., & Baragar, W. R. A. (1971). A guide to the chemical classification of the common volcanic rocks. *Canadian Journal of Earth Sciences*, 8, 523–548.

- James, D. E. (1981). The combined use of oxygen and radiogenic isotopes as indicators of crustal contamination. *Annual Review of Earth and Planetary Sciences*, 9, 311–344.
- Jean, M. M., Shervais, J. W., Choi, S. H., & Mukasa, S. B. (2010). Melt extraction and melt refertilization in mantle peridotite of the Coast Range Ophiolite: An LA-ICP-MS study. *Contribution to Mineralogy and Petrology*, 159, 113–136.
- Jones, H. C. (1934). The iron ore deposits of Bihar and Orissa. *Geological Survey of India, Memoir*, 63(pt.2), 167–302.
- Jourdan, F., Bertrand, H., Scharer, U., Blichert-Toft, J., Feraud, G., & Kampunzu, A. B. (2007). Major and trace element and Sr, Nd, Hf and Pb isotope compositions of the Karoo Large Igneous Province, Botswana Zimbabwe: Lithosphere vs. mantle plume contribution. *Journal of Petrology*, 48, 1043–1077.
- Kaimura, J. I., & Sano, S. (2012). Reactive melt flow as the origin of residual mantle lithologies and basalt chemistries in mid-ocean ridges: Implications from the Red Hills Peridotite, New Zealand. *Journal of Petrology*, 53(8), 1637–1671.
- Kepezhinskas, P., Defant, M. J., & Drummond, M. S. (1995). Na metasomatism in the Island-arc mantle by slab melt–peridotite interaction: Evidence from mantle xenoliths in the North Kamchatka Arc. *Journal of Petrology*, 36, 1505–1527.
- Kepezhinskas, P., Defant, M. J., & Drummond, M. S. (1996). Progressive enrichment of Island arc mantle by melt–peridotite interaction inferred from Kamchatka xenoliths. *Geochimica et Cosmochimica Acta*, 60, 1217–1229.
- Kepezhinskas, P. K., McDermott, F., Defant, M. J., Hochstaedter, A., Drummond, M. S., Hawkesworth, C. J., ... Bellon, H. (1997). Trace element and Sr-Nd-Pd isotopic constraints on a three-component model of Kamchatka arc petrogenesis. *Geochimica et Cosmochimica Acta*, 61, 577–600.
- Kerrick, R., & Manikyamba, C. (2012). Contemporaneous eruption of Nb-enriched basalts - K-adakites - Na-adakites from the 2.7 Ga Penakacherla terrane: Implications for subduction zone processes and crustal growth in the eastern Dharwar Craton, India. *Canadian Journal of Earth Sciences*, 49, 615–636.
- Komiya, T., Yamamoto, S., Aoki, S., Koshida, K., Shimojo, M., Sawaki, Y., & Ishikawa, A. (2017). A prolonged granitoid formation in Saglek Block, Labrador: Zonal growth and crustal reworking of continental crust in the Eoarchean. *Geoscience Frontiers*, 8, 355–385.
- Krishna, A. K., Murthy, N. N., & Govil, P. K. (2007). Multielement analysis of soils by wavelength-dispersive x-ray fluorescence spectrometry. *Atomic Spectroscopy*, 28(6), 202–214.
- Kumar, A., Parashuramulu, V., Shankar, R., & Besse, J. (2017). Evidence for a Neoproterozoic LIP in the Singhbhum Craton, eastern India: Implications to Vaalbara supercontinent. *Precambrian Research*, 292, 163–174.
- Kuno, H. (1964). *Igneous rock series: Chemistry of the Earth's crust 2: Moscow* (pp. 109–121). Moscow: Academy of Science. (in Russian).
- Lassiter, J. C., DePaolo, D. J., & Mahoney, J. J. (1995). Geochemistry of the Wrangellia Flood Basalt Province: Implications for the role of continental and oceanic lithosphere in flood basalt genesis. *Journal of Petrology*, 36, 983–1009.
- Lassiter, J. C., & Luhr, J. F. (2001). Osmium abundance and isotope variations in mafic Mexican volcanic rocks: Evidence for crustal contamination and constraints on the geochemical behaviour of osmium during partial melting and fractional crystallization. *Geochemistry, Geophysics, Geosystems*, 2(3), 1–25.
- Lawrence, R. B., Armstrong, R. E., & Berman, R. G. (1984). Garibaldi Group volcanic rocks of the Salal Creek area, southwestern British Columbia: Alkaline lavas on the fringe of the predominantly calc-alkaline Garibaldi (Cascade) Volcanic Arc. *Journal of Volcanology and Geothermal Research*, 21, 255–276.
- Le Bas, M. J., Le Maitre, R. W., Streckeisen, A., & Zanettin, B. (1986). A chemical classification of volcanic rocks based on the total alkali-silica diagram. *Journal of Petrology*, 27, 745–750.
- LeCheminant, A. N., & Heaman, L. M. (1989). Mackenzie igneous events, Canada: Middle Proterozoic hotspot magmatism associated with ocean opening. *Earth and Planetary Science Letters*, 96, 38–48.
- Liu, Y., Gao, S., Hu, Z., Gao, C., Zong, K., & Wang, D. (2010). Continental and Oceanic Crust Recycling Induced Melt-Peridotite interactions in the Trans-North China Orogen: U-Pb dating, Hf isotopes and trace elements in zircons from mantle xenoliths. *Journal of Petrology*, 51 (1–2), 537–571.
- Mahadevan, T. M. (2002). *Geology of Bihar and Jharkhand*. Bangalore, India: Geological Society of India 563p.
- Mahadevan, T. M. (2008). Precambrian geological and structural features of the Indian Peninsula. *Journal of Geological Society of India*, 72, 35–55.
- Mahoney, J. J. (1988). Deccan Traps. In J. D. Macdougall (Ed.), *Continental Flood Basalts* (pp. 151–194). Dordrecht, the Netherlands: Kluwer Academic Publication.
- Manikyamba, C., Ganguly, S., Santosh, M., & Subramanyam, K. S. V. (2017). Volcano-sedimentary and metallogenic records of the Dharwar greenstone terranes, India: Window to Archean plate tectonics, continent growth, and mineral endowment. *Gondwana Research*, 38, 38–66.
- Manikyamba, C., & Kerrich, R. (2012). Eastern Dharwar Craton, India: Continental lithosphere growth by accretion of diverse plume and arc terranes. *Geoscience Frontiers*, 3(3), 225–240.
- Manikyamba, C., Kerrich, R., Khanna, T. C., Satyanarayanan, M., & Krishna, A. K. (2009). Enriched and depleted arc basalts, with high-Mg andesites and adakites: A potential paired arc-back arc of the 2.7 Ga Hutti greenstone terrane, India. *Geochimica et Cosmochimica Acta*, 73, 1711–1736.
- Manikyamba, C., Pahari, A., Santosh, M., Ray, J., Sindhuja, C. S., Subramanyam, K. S. V., & Singh, M. R. (2020). Mesoarchean gabbro-anorthosite complex from Singhbhum Craton, India. *Lithos*, 366–367, 105541. <https://doi.org/10.1016/j.lithos.2020.105541>
- Manikyamba, C., Ray, J., Ganguly, S., Singh, M. R., Santosh, M., Saha, A., & Satyanarayanan, M. (2015). Boninitic metavolcanic rocks and Island arc tholeiites from the Older Metamorphic Group (OMG) of Singhbhum Craton, eastern India: Geochemical evidence for Archean subduction processes. *Precambrian Research*, 271, 138–159.
- Manikyamba, C., Saha, A., Ganguly, S., Santosh, M., Lingadevaru, M., Singh, M. R., & Subba Rao, D. V. (2014). Sediment-infill volcanic breccia from the Neoproterozoic Shimoga greenstone terrane, Eastern Dharwar Craton: Implications on pyroclastic volcanism and sedimentation in an active continental margin. *Journal of Asian Earth Sciences*, 96, 269–278.
- Mazumder, R., Van Loon, A. J., Mallik, L., Reddy, S. M., Arima, M., Altermann, W., ... De, S. (2012). Mesoarchaeo-Palaeoproterozoic stratigraphic record of the Singhbhum crustal province, eastern India: a synthesis. *Geological Society, London, Special Publications*, 365, 31–49.
- Mc Call, J. G. H. (2003). A critique of the analogy between Archean and Phanerozoic tectonics based on regional mapping of the Mesozoic-Cenozoic plate convergent zone in the Makran, Iran. *Precambrian Research*, 127, 5–18.
- McCarren, J. J., & Smellie, J. L. (1998). Tectonic implications of fore-arc magmatism and generation of high-magnesian andesites: Alexander Island, Antarctica. *Journal of the Geological Society, London*, 155, 269–280.
- Médard, E., Schmidt, M. W., Schiano, P., & Ottoloni, L. (2006). Melting of amphibole-bearing wehrlites: An experimental study on the origin of ultracalcic nepheline-normative melts. *Journal of Petrology*, 47, 481–504.
- Meschede, M. (1986). A method of discriminating between different types of mid-ocean ridge basalts and continental tholeiites with the Nb-Zr-Y diagram. *Chemical Geology*, 56, 207–218.
- Mibe, K., Kawamoto, T., Matsukage, K. N., Fei, Y., & Ono, S. (2011). Slab melting versus slab dehydration in subduction-zone magmatism. *Proceedings of the National Academy of Sciences of the United States of America*, 108(20), 8177–8182.
- Misra, S. (2006). Precambrian chronostratigraphic growth of Singhbhum-Orissa Craton, Eastern Indian shield: An alternative model. *Journal of Geological Society of India*, 67, 356–378.

- Misra, S., Deomurari, M. P., Wiedenbeck, M., Goswami, J. N., Ray, S., & Saha, A. K. (1999). $^{207}\text{Pb}/^{206}\text{Pb}$ zircon ages and the evolution of the Singhbhum Craton, eastern India: An ion microprobe study. *Precambrian Research*, 93, 139–151.
- Mohanty, S. (2012). Spatio-temporal evolution of the Satpura Mountain Belt of India: A comparison with the Capricorn Orogen of Western Australia and implication for evolution of the supercontinent Columbia. *Geoscience Frontiers*, 3, 241–267.
- Morisset, C., Scoates, J. S., & Weis, D. (2006). Trace element and Hf isotopic compositions of magmatic rutile from Fe-Ti oxide ore deposits related to the Proterozoic Anorthosite massifs. *American Geophysical Union (Abstract) Fall meeting*, V33, A0644.
- Morse, S. A. (1980). *Basalts and Phase diagrams: An introduction to the quantitative use of phase diagrams in Igneous Petrology*. New York, NY: Springer-Verlag 493p.
- Mukhopadhyay, D., & Matin, A. (2020). The architecture and evolution of the Singhbhum Craton. *Episodes*, 43, 19–50.
- Mukhopadhyay, J., Beukes, N. J., Armstrong, R. A., Zimmermann, U., Ghosh, G., & Medda, R. A. (2008). Dating the Oldest Greenstone in India: A 3.51 Ga precise U-Pb SHRIMP Zircon Age for Dacitic Lava of the Southern Iron Ore Group, Singhbhum Craton. *Journal of Geology*, 116(5), 449–461.
- Mukhopadhyay, J., Crowley, Q. G., Ghosh, S., Ghosh, G., Chakrabarti, K., Misra, B., ... Bose, S. (2014). Oxygenation of the Archean atmosphere: New paleosol constraints from eastern India. *Geology*, 42, 923–926. <https://doi.org/10.1130/G36091.1>
- Mukhopadhyay, J., Ghosh, G., Zimmermann, U., Guha, S., & Mukherjee, T. (2012). A 3.51 Ga bimodal volcanics-BIF-ultramafic succession from Singhbhum Craton: Implications for Palaeoarchean geodynamic processes from the oldest greenstone succession of the Indian sub-continent. *Geological Journal*, 47, 284–311.
- Mukhopadhyay, J., Gutzmer, J., Beukes, N. J., & Hayashi, K. I. (2008). Stratabound magnetite deposits from the eastern outcrop belt of the Archaean Iron Ore Group, Singhbhum Craton, India. *Applied Earth Science: Transactions of the Institution of Mining and Metallurgy (Section B)*, 117(4), 175–186.
- Mullen, E. D. (1983). MnO/TiO₂/P₂O₅: A major element discriminant for basaltic rocks of oceanic environments and its implication for petrogenesis. *Earth and Planetary Science Letters*, 62, 53–62.
- Nelson, D. R., Bhattacharya, H. N., Thern, E. R., & Altermann, W. (2014). Geochemical and ion-microprobe U-Pb zircon constraints on the Archaean evolution of Singhbhum Craton, eastern India. *Precambrian Research*, 255, 412–432.
- Niu, Y., & O'Hara, M. J. (2003). Origin of ocean Island basalts: A new perspective from petrology, geochemistry and mineral physics considerations. *Journal of Geophysical Research*, 108(B4), ECV 5-1–ECV 5-19. <https://doi.org/10.1029/2002JB002048>.
- Pahari, A., Tang, L., Manikyamba, C., Santosh, M., Subramanyam, K. S. V., & Ganguly, S. (2019). Meso-Neoproterozoic magmatism and episodic crustal growth in the Kudremukh-Agumbe granite-greenstone belt, western Dharwar Craton, India. *Precambrian Research*, 323, 16–54.
- Pearce, J. A. (2008). Geochemical fingerprinting of oceanic basalts with applications to ophiolite classification and the search for Archean oceanic crust. *Lithos*, 100, 14–48.
- Pearce, J. A., & Cann, J. R. (1973). Tectonic setting of basic volcanic rocks determined using trace element analyses. *Earth and Planetary Science Letters*, 19, 290–300.
- Pearce, T. H., Gorman, B. E., & Birkett, T. C. (1977). The relationship between major element chemistry and tectonic environment of basic and intermediate volcanic rocks. *Earth and Planetary Science Letters*, 36, 121–132.
- Polat, A., Hofmann, A. W., & Rosing, M. T. (2002). Boninite-like volcanic rocks in the 3.7–3.8 Ga Isua greenstone belt, West Greenland: Geochemical evidence for intra-oceanic subduction zone processes in the early Earth. *Chemical Geology*, 184, 231–254.
- Polat, A., & Kerrich, R. (2001). Magnesian andesites, Nb-enriched basalt-andesites, and adakites from Late Archean 2.7 Ga Wawa greenstone belts, Superior Province, Canada: Implications for late Archean subduction zone petrogenetic processes. *Contribution to Mineralogy and Petrology*, 141, 36–52.
- Polat, A., & Kerrich, R. (2006). Reading the geochemical fingerprints of Archean hot subduction volcanic rocks: Evidence for accretion and crustal recycling in a mobile tectonic regime. In K. Benn, J. C. Mareschal, & K. C. Condie (Eds.), *Archean geodynamics and environments* (Vol. 164, pp. 189–213). Washington D.C.: American Geophysical Union, Geophysical Monograph.
- Polat, A., Kerrich, R., & Wyman, D. A. (1999). Geochemical diversity in oceanic komatiites and basalts from the late Archaean Wawa greenstone belts, Superior Province, Canada: Trace element and Nd isotopic evidence for a heterogeneous mantle. *Precambrian Research*, 94, 139–173.
- Prat, F. C., Ganne, J., & Lombard, A. (2003). No significant element transfer from the oceanic plate to the mantle wedge during subduction and exhumation of the Tethys lithosphere (Western Alps). *Lithos*, 69(3-4), 69–103.
- Prouteau, G., Scaillet, B., Pichavant, M., & Maury, R. (2001). Evidence for mantle metasomatism by hydrous silicic melts derived from subducted oceanic crust. *Nature*, 410, 197–200.
- Rapp, R. P., Shimizu, N., Norman, M. D., & Applegate, G. S. (1999). Reaction between slab-derived melts and peridotite in the mantle wedge: Experimental constraints at 3.8 GPa. *Chemical Geology*, 160, 335–356.
- Ray, J., Saha, A., Koeberl, C., Thoni, M., Ganguly, S., & Hazra, S. (2013). Geochemistry and petrogenesis of Proterozoic mafic rocks from East Khasi Hills, Shillong Plateau, Northeastern India. *Precambrian Research*, 230, 119–137.
- Reichow, M. K., Saunders, A. D., White, R. V., Al'Mukhamedov, A. I., & Medvedev, A. Y. (2005). Geochemistry and petrogenesis of basalts from the West Siberian Basin: An extension of the Permo-Triassic Siberian Traps, Russia. *Lithos*, 79, 425–452.
- Rey, P. F., Philippot, P., & Thebaud, N. (2003). Contribution of mantle plumes, crustal thickening and greenstone blanketing to the 2.75–2.65 Ga global crisis. *Precambrian Research*, 127, 43–60.
- Roedder, E. (1951). Low temperature liquid immiscibility in the system of K₂O-FeO-Al₂O₃-SiO₂. *American Mineralogist*, 36, 282–286.
- Roy, A. B., & Bhattacharya, H. N. (2012). Tectonostratigraphic and geochronological reappraisal constraining the growth and evolution of Singhbhum Archaean Craton, Eastern India. *Journal of Geological Society of India*, 80, 455–469.
- Saha, A. K. (1994). Crustal evolution of Singhbhum-North Orissa, Eastern India. *Geological Society of India, Memoir*, 27 341p.
- Saha, A. K., Ray, S. L., & Sarkar, S. N. (1988). Early history of the Earth: Evidence from the Eastern Indian shield. In D. Mukhopadhyay (Ed.), *Precambrian of the Indian shield* (Vol. 8, pp. 13–37). Bangalore, India: Geological Society of India, Memoir.
- Saha, D., & Mazumder, R. (2012). An overview of the Palaeoproterozoic geology of Peninsular India, and key stratigraphic and tectonic issues. *Geological Society, London, Special Publications*, 365(1), 5–29.
- Saha, L., Hofmann, A., & Xie, H. (2012). Archaean evolution of the Singhbhum Craton: Constraints from new metamorphic-geochemical data and SHRIMP zircon ages. In *Craton formation and destruction with special emphasis on BRICS cratons* (pp. 7–9). South Africa: University of Johannesburg.
- Sajona, F. G., Maury, R. C., Bellon, H., Cotton, J., & Defant, M. J. (1996). High field strength element enrichment of Pliocene-Pleistocene Island arc basalts, Zamboanga Peninsula, Western Mindanao (Philippines). *Journal of Petrology*, 37, 693–726.
- Sajona, F. G., Maury, R. C., Bellon, H., Cotton, J., Defant, M. J., & Pubellier, M. (1993). Initiation of subduction and the generation of slab melts in western and eastern Mindanao, Philippines. *Geology*, 21, 1007–1010.

- Santosh, M. (2013). Evolution of continents, cratons and supercontinents: Building the habitable Earth. *Current Science*, 104, 871–879.
- Sarkar, S. N., & Saha, A. K. (1962). A revision of the Precambrian stratigraphy and tectonics of Singhbhum and adjacent region. *Quarterly Journal, Geological Mining and Metallurgical Society of India*, 34, 97–136.
- Sarkar, S. N., & Saha, A. K. (1963). On the occurrence of two intersecting Precambrian orogenic belts in Singhbhum and adjacent areas, India. *Geological Magazine*, 100, 69–92.
- Sengupta, S., Acharyya, S. K., & Deshmeth, J. B. (1997). Geochemistry of Archaean volcanic rocks from Iron Ore Supergroup, Singhbhum, eastern India. *Proceedings of the Indian Academy of Sciences (Earth Planetary Science)*, 106, 327–342.
- Sengupta, S., Corfu, F., McNutt, R. H., & Paul, D. K. (1996). Mesoarchaean crustal history of the eastern Indian craton: Sm-Nd and U-Pb isotopic evidence. *Precambrian Research*, 77, 17–22.
- Shankar, R., Srinivasa Sarma, D., Ramesh Babu, N., & Parashuramulu, V. (2018). Palaeomagnetic study of 1765 Ma dyke swarm from Singhbhum Craton: Implications to the palaeogeography of India. *Journal of Asian Earth Sciences*, 157, 235–244.
- Sharma, R. S. (2009). *Cratons and fold belts of India*. Heidelberg, Germany: Springer Verlag 322p.
- Singh, M. R., Manikyamba, C., Ray, J., Ganguly, S., Santosh, M., Saha, A., ... Sawant, S. S. (2016). Major, trace and platinum group element (PGE) geochemistry of Archean Iron Ore Group and Proterozoic Malangtoli metavolcanic rocks of Singhbhum Craton, Eastern India: Inferences on mantle melting and sulphur saturation history. *Ore Geology Reviews*, 72, 1263–1289.
- Smithies, R. H., Champion, D. C., Van Kranendonk, M. J., Howard, H. M., & Hickman, A. H. (2005). Modern-style subduction processes in the Mesoarchaean. Geochemical evidence from the 3.12 Ga Whundo intra-oceanic arcs. *Earth and Planetary Science Letters*, 231, 221–237.
- Soderlund, U., Elmings, S.-A., Ernst, R. E., & Schissel, D. (2006). The Central Scandinavian Dolerite Group: Protracted hotspot activity or back-arc magmatism? Constraints from U-Pb baddeleyite geochronology and Hf isotope data. *Precambrian Research*, 150, 136–152.
- Sreenivas, B., Dey, S., Bhaskar Rao, Y. J., Vijaya Kumar, T., Babu, E. V. S. K., & Williams, I. S. (2019). A new cache of Eoarchaean detrital zircons from the Singhbhum Craton, eastern India and constraints on early Earth geodynamics. *Geoscience Frontiers*, 10(4), 1359–1370.
- Srivastava, R. K., & Ahmad, T. (2008). Precambrian mafic magmatism in the Indian Shield: An introduction. *Journal of Geological Society of India*, 72, 9–13.
- Srivastava, R. K., Söderlund, U., Ernst, R. E., Mondal, S. K., & Samal, A. K. (2016). Neoarchaean-Palaeoproterozoic mafic dyke swarms from the Singhbhum Granite Complex, Singhbhum Craton, eastern India: Implications for identification of large igneous provinces and their possible continuation on other formerly adjacent crustal blocks. *Acta Geologica Sinica (English Edition)*, 90(supp. 1), 17–18.
- Stern, C. R., & Kilian, R. (1996). Role of the subducted slab, mantle wedge and continental crust in the generation of adakites from the Austral Volcanic zone. *Contribution to Mineralogy and Petrology*, 123, 263–281.
- Sun, S. S., & McDonough, W. F. (1989). Chemical and isotopic systematics of oceanic basalts: Implications for mantle composition and processes. In A. D. Saunders & M. J. Norry (Eds.), *Magmatism in the Ocean Basins* (Vol. 42, pp. 313–345). London: Geological Society of London Special Publication <https://doi.org/10.1144/GSL.SP.1989.042.01.19>
- Suominen, V. (1991). The Chronostratigraphy of Southwestern Finland with special reference to Postjotnian and Subjotnian diabbases. *Geological Survey of Finland, Bulletin*, 356 106p.
- Sylvester, P. J., Campbell, I. H., & Bowyer, D. A. (1997). Niobium/Uranium evidence for early formation of the continental crust. *Science*, 275, 521–523.
- Tait, J., Zimmermann, U., Miyazaki, T., Presnyakov, S., Chang, Q., Mukhopadhyay, J., & Sergeev, S. (2011). Possible juvenile Palaeoarchaean TTG magmatism in eastern India and its constraints for the evolution of the Singhbhum Craton. *Geological Magazine*, 148, 340–347.
- Tatsumi, Y. (2006). High-Mg andesites in the Setouchi volcanic belt, southwestern Japan: Analogy to Archean magmatism and continental crust formation? *Annual Reviews, Earth and Planetary Sciences*, 34, 467–499.
- Thomson, A. R., Walter, M. J., Kohn, S. C., & Brooker, R. A. (2016). Slab melting as a barrier to deep carbon subduction. *Nature*, 529, 76–79.
- Thornton, C. P., & Tuttle, O. F. (1960). Chemistry of igneous rocks: Pt. 1. Differentiation index. *American Journal of Science*, 258, 664–684.
- Thurston, P. C. (1990). Early Precambrian basic rocks of the Canadian Shield. In R. P. Hall & D. J. Hughes (Eds.), *Early Precambrian basic magmatism* (pp. 221–247). Springer, Dordrecht: Blackie and Son Limited.
- Turkina, O. M., & Nozhkin, A. D. (2003). Genesis of Archean tonalite-trondhjemite suites: Plume or subduction related? *Russian Journal of Earth Sciences*, 5, 93–100.
- Upadhyay, D., Chattopadhyay, S., Kooijman, E., Mezger, K., & Berndt, J. (2014). Magmatic and metamorphic history of Palaeoarchaean tonalite-trondhjemite-granodiorite (TTG) suites from the Singhbhum Craton, Eastern India. *Precambrian Research*, 252, 180–190.
- Upton, B. G. J., Emeleus, C. H., Heaman, L. M., Goodenough, K. M., & Finch, A. A. (2003). Magmatism of the mid-Proterozoic Gardar Province, South Greenland: Chronology, petrogenesis and geological setting. *Lithos*, 68, 43–65.
- Walowski, K. J., Wallace, P. J., Hauri, E. H., Wada, I., & Clyne, M. A. (2015). Slab melting beneath the Cascade Arc driven by dehydration of altered oceanic peridotite. *Nature Geoscience*, 8, 404–408.
- Weaver, B. L. (1991). The origin of ocean island basalt end-member compositions: Trace element and isotopic constraints. *Earth and Planetary Science Letters*, 104, 381–397.
- Wilde, S. A., Zhou, X. H., Nemchin, A. A., & Sun, M. (2003). Mesozoic crust–mantle interaction beneath the North China Craton: A consequence of the dispersal of Gondwanaland and accretion of Asia. *Geology*, 31(9), 817–820.
- Wilson, M. (1989). *Igneous Petrogenesis*. London, UK: Unwin Hyman 466p.
- Wingate, M. T. D. (1999). Ion microprobe baddeleyite and zircon ages for Late Archaean mafic dykes of the Pilbara Craton, Western Australia. *Australian Journal of Earth Sciences*, 46, 493–500.
- Wood, D. A. (1980). The application of a Th-Hf-Ta diagram to problems of tectonomagmatic classification and to establish the nature of crustal contamination of basaltic lavas of the Tertiary Volcanic Province. *Earth and Planetary Science Letters*, 50, 11–30.
- Wyman, D. (2018). Do cratons preserve evidence of stagnant lid tectonics? *Geoscience Frontiers*, 9, 3–17.
- Wyman, D. A., Ayer, J. A., & Devaney, J. R. (2000). Niobium-enriched basalts from the Wabigoon subprovince, Canada: Evidence for adakitic metasomatism above an Archean subduction zone. *Earth and Planetary Science Letters*, 179, 21–30.
- Zhai, M. (2014). Multi-stage crustal growth and cratonization of the North China Craton. *Geoscience Frontiers*, 5(4), 457–469.

SUPPORTING INFORMATION

Additional supporting information may be found online in the Supporting Information section at the end of this article.

How to cite this article: Paul M, Ray J, Manikyamba C, et al. Mafic volcanic rocks of western Iron Ore Group, Singhbhum Craton, eastern India: Geochemical evidence for ocean–continent convergence. *Geological Journal*. 2020;1–28. <https://doi.org/10.1002/gj.3944>